Radiative transfer Vcmax estimation from hyperspectral imagery and SIF retrievals to assess photosynthetic performance in rainfed and irrigated plant phenotyping trials

Carlos Camino[a], Victoria Gonzalez-Dugo[a], Pilar Hernandez[a], Pablo J. Zarco-Tejada[b,c,a,*]

[a] *Instituto de Agricultura Sostenible (IAS), Consejo Superior de Investigaciones Científicas (CSIC), Córdoba, Spain*
[b] *School of Agriculture and Food, Faculty of Veterinary and Agricultural Sciences (FVAS), University of Melbourne, Melbourne, Victoria, Australia*
[c] *University of Melbourne, Melbourne, Victoria, Australia*

ARTICLE INFO

ABSTRACT

Plant photosynthetic traits may be indicative of stress tolerance and performance in the field, making their accurate assessment critical in phenotyping trials. The maximum rate of carboxylation (Vcmax) is a key parameter for estimating CO_2 assimilation (A), as it controls the CO_2 fixation rate. This study demonstrates the utility of combining airborne-based solar-induced chlorophyll fluorescence (SIF) and hyperspectral imagery through the inversion of the Soil-Canopy Observation of Photosynthesis and Energy (SCOPE) model to estimate Vcmax, using sensor resolutions available in precision agriculture technologies. Vcmax was quantified in three wheat phenotyping experimental fields during the 2015–2018 growing seasons, comprising both rainfed and irrigated conditions. Airborne campaigns were carried out with two hyperspectral sensors, covering the 400–850 nm (20 cm resolution) and 950–1750 nm (70 cm resolution) spectral regions, and with a thermal camera (25 cm resolution) in the 8–14 μm region. Validation between model-estimated and field-measured Vcmax was statistically significant ($r^2 = 0.77$; p-value $\leq 2.2e-16$), and Vcmax was reliably associated with net assimilation both in irrigated and rainfed conditions ($r^2 = 0.65$ and 0.5, respectively). By contrast, simulated chlorophyll content (Cab) and airborne-derived structural and chlorophyll indicators (NDVI and PSSRb) lacked significant correlations with assimilation rate in irrigated plots, while the relationship between assimilation rate and the crop water stress index (CWSI) was not significant in rainfed plots. The superior sensitivity of remotely-sensed Vcmax under irrigated conditions was likely related to its robustness to distortions from high canopy densities observed in other indices. The remote sensing retrieval of Vcmax, and the methodology demonstrated in this study is directly relevant for high-throughput plant phenotyping and for precision agriculture applications.

1. Introduction

CO_2 assimilation (A) occurs in the chloroplasts and involves light biochemical reactions (Quebbeman and Ramirez, 2016). Environmental conditions such as light intensity and temperature, biophysical processes such as CO_2 transport through the leaf and stomata, and leaf biochemistry determine the assimilation rate (Sharkey et al., 2007). At the leaf level, the photosynthetic capacity is defined by the maximum rate of carboxylation (Vcmax) and the maximum rate of electron transport (Jmax). Vcmax is the maximum rate of Ribulose−1,5-Bisphosphate (RuBP) carboxylation, which controls CO_2 fixation (Farquhar et al., 1980). Jmax is the maximum rate of electron transport, which limits the supply of ATP and NADPH during the carboxylation and the regeneration of RuBP in the Calvin-Benson cycle (Quebbeman

and Ramirez, 2016). Wullschleger (1993) demonstrated that Jmax should follow Vcmax across plant species, a relationship not affected by nitrogen content within leaves (Walker et al., 2014).

The most common biochemical photosynthesis model for estimating the CO_2 assimilation at leaf level is the Farquhar–von Caemmerer–Berry (FvCB) model (Farquhar et al., 1980). The FvCB model and its subsequent variants (Caemmerer and Farquhar, 1981; Farquhar and Wong, 1984; Collatz et al., 1992; Harley et al., 1992a) relate the kinetic properties of Ribulose-1,5-Bisphosphate Carboxylase-Oxygenase (RuBisCo) to photosynthetic capacity (Caemmerer, 2000). The FvCB model is typically embedded in terrestrial biosphere models (TBM), which have been used to estimate photosynthetic carbon uptake (Norton et al., 2017), gross primary productivity (Sellers, 1987; Koffi et al., 2015) and leaf respiration (Sitch et al., 2003; Oleson et al., 2013). In recent years,

---

* Corresponding author at: University of Melbourne, Melbourne, Victoria, Australia.
*E-mail address:* pablo.zarco@unimelb.edu.au (P.J. Zarco-Tejada).
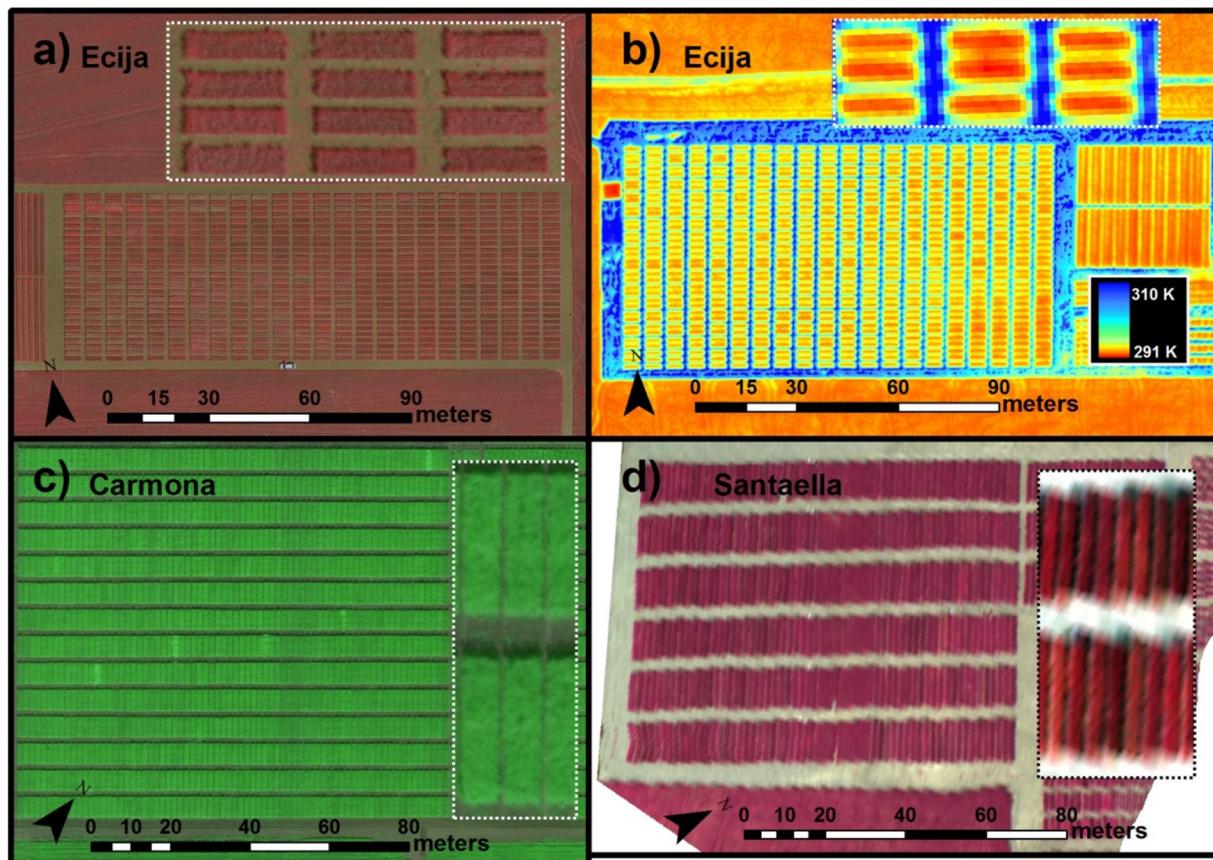
Fig. 1. Overview of the field trial sites at Ecija (a and b), Carmona (c) and Santaella (d). Figures a and c were obtained with a CIR camera (a: 800 (R), 670 (G) and 550 (B) nm; d: true color). Figure b shows a sample of the thermal imagery. Figure d was obtained with a VNIR hyperspectral imager (composite: 706 (R), 679 (G) and 520 (B) nm).

progress has been made to quantify photosynthetic capacity from hyperspectral satellite imagery, enabling the development of TBMs at new spatial scales. In the context of a plant phenotyping study, Silva-Perez et al. (2018) demonstrated the use of hyperspectral reflectance to estimate Vcmax and other physiological traits in wheat crops. However, imagery was obtained at the leaf level, where the remote sensing signal was not affected by canopy structure, as it is for larger-scale applications. For images at the canopy level, standard reflectance indices such as the normalized difference vegetation index (NDVI) (Rouse et al., 1973) have been widely used for detecting vigor, growth, yield and senescence patterns from airborne and near-field scales in maize and wheat crops (Cairns et al., 2012; Kipp et al., 2014). However, NDVI has well-known disadvantages associated with its saturation at high biomass levels, its sensitivity to canopy background, and the inability to track short-term physiological changes due to its strong relationship with tissue structure (Huete, 1988; Huete et al., 2002). Despite these disadvantages, NDVI is still one of the most widely used indicators for the remote assessment of canopy characteristics by plant breeders.

Several studies have demonstrated that canopy temperature can be related to physiological processes (Gonzalez-Dugo et al., 2015) or even used to detect nutritional deficiencies (Rodriguez et al., 2006). The thermal-based Crop Water Stress Index (CWSI) developed by Idso et al. (1978) and Jackson et al. (1981) is inversely related to transpiration and stomatal conductance, and therefore a potentially good proxy for estimating crop photosynthesis rates under stress. However, a range of environmental factors may affect the relationship between stomatal closure and canopy temperature, such as changes in radiation exposure, nutrient deficiency or soil water deficit (Radin et al., 1985; Jones et al., 1995; Zweifel et al., 2002).

In the last twenty years the quantification of sun-induced

chlorophyll fluorescence (SIF) through hyperspectral imaging has provided a new tool for monitoring crop photosynthetic activity and vegetation functioning (Frankenberg et al., 2011; Houborg et al., 2013; Zarco-Tejada et al., 2016; Norton et al., 2017). Chlorophyll fluorescence is closely related to the electron transport rate and hence to photosynthetic activity (Genty et al., 1989; Weis and Berry, 1987). Chlorophyll fluorescence may therefore be useful for detecting nutrient-limitation in crops (Camino et al., 2018a). Chlorophyll fluorescence may also be used to estimate Vcmax since both are linked with chlorophyll content (Houborg et al., 2013; Croft et al., 2017) and therefore photosynthetic activity (Rascher et al., 2015; Yang et al., 2015).

Recent studies have successfully estimated Vcmax from satellite SIF retrievals (Guan et al., 2016; Zhang et al., 2014, 2018) using the Soil Canopy Observation, Photochemistry and Energy fluxes (SCOPE) model (Guanter et al., 2014; Koffi et al., 2015; Zhang et al., 2014, 2018). Nevertheless, further progress is needed for the assessment of Vcmax under both water and nutrient-limited conditions (i.e. under stress) and in the context of plant phenotyping experiments with high-resolution imagery. In some cases, SIF retrievals have been performed using cost-effective hyperspectral imagers with broader spectral resolutions (i.e. 2–7 nm FWHM) (Damm et al., 2015; Zarco-Tejada et al., 2016; Camino et al., 2018b). Although offsets in the fluorescence retrievals may occur due to the broader spectral resolutions used in these imagers, the consequences may be negligible for most precision agriculture applications since emphasis is on relative spatio-temporal variability of stress rather than absolute fluorescence emission levels.

The remote assessment of plant photosynthesis requires careful attention to the influence of stress. Photosynthesis is strongly affected by stress, with assimilation affected by water deficit (Chaves, 1991) and carboxylation capacity sensitive to leaf nitrogen levels (Walker et al.,

2014). However, under drought conditions, water deficit may alter the nitrogen balance as growth rate diminishes (Gonzalez-Dugo et al., 2010). In bread wheat, populations display heritable variation in photosynthetic traits, amenable to artificial selection (Carmo-Silva et al., 2017). As a result, remotely sensed chlorophyll fluorescence may be useful for phenotyping photosynthetic traits desirable for breeding. In this study we quantify Vcmax as a proxy for photosynthetic activity in wheat phenotyping trials using airborne hyperspectral-based SIF retrievals through SCOPE model inversions. Specifically, we evaluated airborne estimates of Vcmax under both well-watered and water-limited regimes.

2. Material and methods

2.1. Study area

Experiments took place at three field trial sites for bread wheat (*Triticum aestivum* L.) and durum wheat (*Triticum turgidum* L. *var. durum*) in Southern Spain in 2015, 2016 and 2018 (Fig. 1). The regional climate is Mediterranean, characterized by mild winters, warm and dry summers and with annual rainfall averages around 600 mm. The first trial site was located in Ecija (37°32′17″N, 5°06′57″W), which was managed under rainfed conditions in 2015 and 2018. The plot size was 12.5 m^2 (10 m × 1.25 m) with a spacing of 1 m × 1.25 m between plots (Fig. 1a and d).

The second site trial was located in Carmona (37°30′29″N, 5°34′42″W) in 2015, which was managed under both rainfed and irrigated conditions. Severe drought at the Carmona experimental site during the spring of 2015 (precipitation < 30 mm in preceding months of the airborne campaign) prompted irrigation in rainfed plots the week before the flights to partially recover the experiment and to avoid damage. At Carmona, 882 individual plots (7.5 × 1.25 m) were divided across two blocks according to water regime. There was a space of 1.50 m × 0.25 m between plots (Fig. 1b). Forty-nine varieties of durum or bread wheat were replicated three times per block.

The third trial site was located in Santaella (37°31′34″N, 4°50′40″W), which was also managed under rainfed and irrigated conditions in 2016. Twenty varieties of durum wheat and 20 varieties of bread wheat were replicated three times across a total of 120 plots (Fig. 1c). The plot size was 15 m^2 (10 × 1.5 m) with a spacing of 2.50 m × 0.50 m between plots.

At all trial sites, plots consisted of five rows of wheat with a spacing of 0.25 cm per row. Physiological measurements and spectral reflectance were taken from the three central rows. The remaining two rows were excluded from analysis. The soil in the three trial sites was dominated by vertisols (FAO classification), which ranged in texture from clay, clay loam to silt. Slope across sites ranged from 2 to 4%. Vertisols are often poor in organic matter and associated with nitrogen and phosphorus deficiencies. Fertilization with diammonium phosphate and urea was carried out in early November to ensure fertility levels.

The wheat growth stage during the airborne campaigns corresponded to i) stem elongation stage, and ii) the grain filling (milking stage) (Table 1). All flights were performed under clear sky conditions. Average meteorological conditions during each flight (ERA-Interim atmospheric reanalysis data; http://www.ecmwf.int) are presented in Table 1.

2.2. Field physiological measurements and leaf gas exchange curves

A summary of the physiological variables measured for each site and sampling date is included in Table 1. Field measurements of assimilation rate (A; μmol·m^{-2}·s^{-1}) and leaf water potential (ψL; MPa) were made at the same time (± 1 h) as acquisition of high-resolution airborne imagery over the experimental field sites. These measurements were performed on leaves at the top of the canopy at noontime, under clear skies and with photosynthetically active radiation (PAR) values

ranging from 1700 to 2200 μmol·m^{-2}·s^{-1}. To assess the physiology and nutritional status of the wheat plots under different water regimes, some additional leaf measurements were made at the trial sites (Table 1). Leaf photosynthesis was measured with a photosynthesis measurement system (LC pro- SD, ADC Bioscientific Ltd., Herts, UK) on two leaves per plot. The LCpro-SD plant leaf photosynthesis chamber has a flow rate accuracy of ± 2% of its range. Leaf water potential (ψL) was measured on two sunlit leaves per plot with a pressure chamber (Model 600 Pressure Chamber Instrument, PMI Instrument Company, Albany, NY, USA). Chlorophyll content was measured on 10–15 leaves per plot using a hand-held chlorophyll meter (SPAD-502, Minolta Corp., Ramsey, NJ, USA). The SPAD-502 chlorophyll meter has an accuracy of ± 1 SPAD units. In 2018, leaf chlorophyll content was measured with the Dualex instrument (FORCE-A, Orsay, France), which has an accuracy of 5%. The SPAD and Dualex readings were converted to chlorophyll content (μg·cm^{-2}) according to Uddling et al. (2007). Total N concentration (%) was determined by the Kjeldahl method (Kjeldahl, 1883) in random samples of 20–25 leaves from the top of the canopy in select plots. This value was demonstrated to be a good proxy of the crop nutritional status (Farruggia et al., 2004).

The response of assimilation to intercellular CO_2 concentration was measured using the portable LCpro-SD photosynthesis measurement system during the field campaign at Ecija in 2018. To assess variability in CO_2 response curves, six wheat varieties (W$_I$ to W$_{VI}$) displaying contrasting nutritional and physiological statuses were selected across the trial site (Fig. 2). Varieties were selected based on patterns in chlorophyll content, nitrogen, and assimilation rate (red asterisks in Fig. 2). The photosynthetic photon flux density was kept constant at 1900 μmol·m^{-2}·s^{-1} during measurements. Prior to sampling, selected leaves were adapted to the chamber light conditions, humidity and temperature for about 5 min. CO_2 concentration was then ramped in steps of 100 ppm, with each step lasting a minimum of 1 min and a maximum of 3 min.

Leaf Vcmax was estimated from assimilation-intercellular CO_2 concentration (A-C$_i$) curves (Fig. 3) using the C$_3$ FvCB photosynthesis model (Farquhar et al., 1980). Photosynthetic response [CO_2] curves developed by Sharkey et al. (2007) were used to estimate Vcmax according to the FvCB model. Following this method, field measurements with intercellular CO_2 partial pressure between 20 and 30 Pa were excluded to reduce errors associated with the interface between the RuBisCo-limited and RuBP-regeneration-limited state.

Kinetic parameters for respiration (R$_d$) and the mesophyll conductance (g$_m$) were estimated for each wheat variety following the nonlinear curve fitting procedures outlined in Sharkey et al. (2007). The temperature dependence of the Michaelis-Menten constant of RuBisCo (K$_c$) for CO_2, inhibition constant (K$_o$), photorespiratory compensation point (Γ*), R$_d$, g$_m$, Vcmax, rate of photosynthetic electron transport (J) and triose phosphate use (TPU) were estimated using exponential functions of temperature responses described in Harley et al. (1992b). The scaling constant (c), enthalpies of activation (ΔH$_a$), deactivation (ΔH$_d$) and entropy (ΔS) were taken from Sharkey et al. (2007) in Table 1.

The retrievals of Vcmax were adjusted to 25 °C using the FvCB model. Only measurements where leaf temperatures were ± 0.5 °C of the average were used in generating these estimates. Atmospheric pressure and intercellular concentration of oxygen (O$_i$) for all collected wheat varieties were set to 21 kPa and 99.75 kPa, respectively. R$_d$ and g$_m$ values used to estimate Vcmax are provided in Table 2.

2.3. Airborne campaigns

Five airborne campaigns were conducted using an aircraft operated by the Laboratory for Research Methods in Quantitative Remote Sensing (QuantaLab), Consejo Superior de Investigaciones Científicas (IAS-CSIC, Spain). Flights occurred at 250 m above ground level (AGL) with heading on the solar plane. Images were acquired concurrently

Table 1

Flight dates and field measurements collected during the airborne campaigns. The meteorological conditions at the time of the flights are included.

Year	Site	Flight dates	Growth stage	Airborne imagery	Field measurements	Meteorological conditions		
						T_a	RH	R_{in}
2015	Ecija	28/05	Grain filling	T + VNIR + NIR	ψ_L, A, C_{ab}, N	295.1	38.0	944.2
	Carmona	30/05	Grain filling	T + VNIR + NIR	ψ_L, A, C_{ab}, N	296.8	38.8	935.8
2016	Santaella	17/03	Stem elongation	T + VNIR + NIR	ψ_L, A, C_{ab}, N	289.6	49.2	558.2
	Santaella	26/04	Grain filling	T + VNIR + NIR	ψ_L, A, C_{ab}, N	297.5	42.5	933.3
2018	Ecija	18/04	Stem elongation	T + VNIR + NIR	A, Cab, N, Curve A/C_i	297.1	43.6	924.8

T = thermal, VNIR = hyperspectral visible and infrared region, NIR = hyperspectral near-short wave infrared region,
ψ_L = leaf water potential (MPa), A = net assimilation rate ($\mu\cdot$mol$\cdot$m$^{-2}\cdot$s^{-1}), C_{ab} = chlorophyll content (μg$\cdot$cm^{-2}),
N = nitrogen concentration (%), Curve A/Ci = response curves of A to the intercellular CO_2 concentration,
T_a = air temperature (K), RH = relative humidity (%) and R_{in} = Incoming shortwave radiation (W$\cdot$m^{-2}).

with field data acquisitions (Table 1) between 12:00 and 13:00 h (local time) under clear sky conditions and free of coarse aerosol (i.e.: dust mineral, biomass burning). To minimize differences due to sun angle effects, the flights were performed at solar zenith angle between 45° and 60°, which varied according to the day, place and the exact flight time. The viewing zenith angle was 0° for all flights. Images were collected with a micro-hyperspectral imager (Micro-Hyperspec VNIR model, Headwall Photonics, Fitchburg, MA, USA), a Micro-Hyperspec NIR-100 (Headwall Photonics) and a thermal infrared camera (FLIR SC655, FLIR Systems, Wilsonville, OR, USA). The Micro-Hyperspec VNIR was configured to acquire 260 spectral bands with a light dispersion of 1.85 nm/pixel with 12-bit radiometric resolution in the 400–885 nm spectral region, yielding a 6.4 nm full width at half maximum (FWHM) with an entrance slit width of 25-μm. The acquisition and storage module obtained 50 frames per second at 25 ms integration time. The 8-mm focal length lens yielded an IFOV of 0.93 mrad and an angular FOV of 50° with a spatial resolution of 20 cm (Fig. 1c). The micro-hyperspec NIR-100 sensor was configured for 165 spectral bands at 16-bit radiometric resolution covering the 950–1750 nm spectral region, yielding 6.05 nm FWHM with a spatial resolution of 70 cm. Radiometric calibration of the VNIR and NIR-100 cameras was performed with an integrating sphere (CSTM-USS-2000C LabSphere, North Sutton, NH, USA) using four levels of illumination and six integration times.

Hyperspectral imagery was atmospherically corrected using
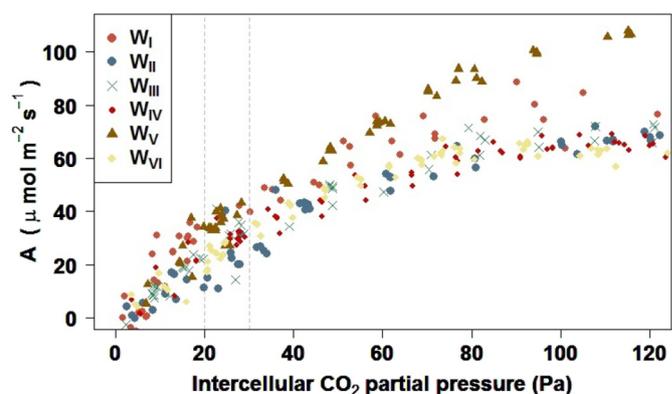
Fig. 3. Relationship obtained between assimilation rate (A; μmol$\cdot$m$^{-2}\cdot$s^{-1}) and intercellular CO_2 partial pressure (Pa). Each color is associated with different wheat varieties (W_n). The dashed lines represent the RuBisCo-limited (left) and RuBP-regeneration-limited (right) state according to Sharkey et al. (2007).

incoming irradiance measured with a field spectrometer (FieldSpec Handheld Pro, ASD Inc., Longmont, Colorado, USA) for the VNIR sensor, and simulated by the SMARTS model (Gueymard, 1995; Gueymard et al., 2002) for the NIR-100 sensor. In addition, the view and illumination angle effects were corrected using a bidirectional
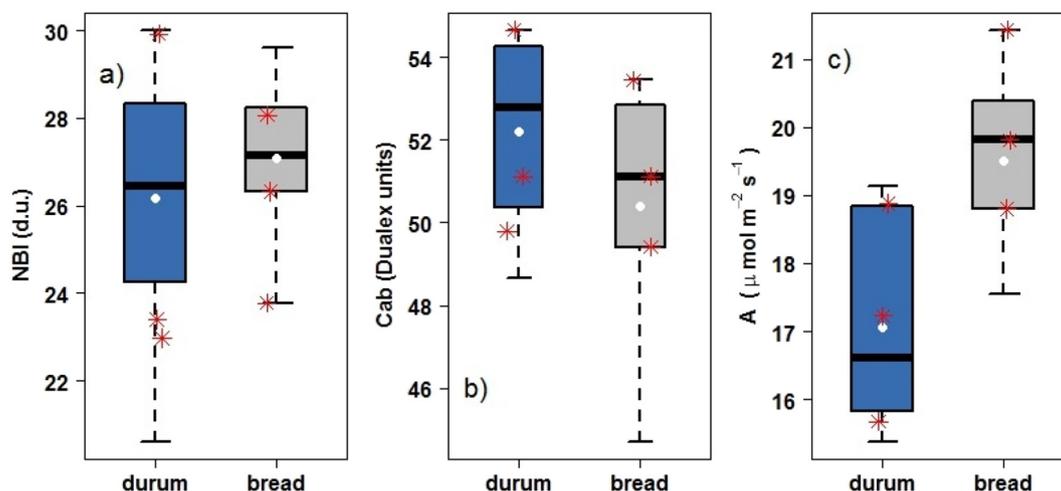
Fig. 2. Leaf physiological measurements on durum wheat plots (in blue) and bread wheat plots (in grey) carried out during the field campaign in Ecija 2018 under rainfed conditions: a) the nitrogen balance index (NBI) in dimensionless units (d.u.), b) chlorophyll content (C_{ab}) in Dualex units (both measurements were collected with the hand-held Dualex device) and c) assimilation rate (A) in μmol$\cdot$m$^{-2}\cdot$s^{-1}, measured with the plant leaf photosynthesis chamber. The red asterisks indicate wheat plots selected for A/Ci curves. In the box plots, the black line within the box is the median, and the top and bottom of the box represent the 75th and 25th quartiles, respectively. The whiskers represent the upper and lower range. The average values are shown with a white point over each box plot. (For interpretation of the references to color in this figure legend, the reader is referred to the web version of this article.)

Table 2
Input parameters and constants (adjusted to 25 °C), maximum carboxylation rate (Vcmax), photosynthetic electron transport rate (J) and triose phosphate use (TPU) obtained from the A/Ci curves shown in Fig. 3 for six wheat varieties using exclusively measures with a leaf temperature equal to the average ± 0.5 °C. The kinetic parameters include the Michaelis constant of RuBisCo for carbon dioxide (K_c), the inhibition constant (K_o), and the photorespiratory compensation point (Γ^*). Day respiration (R_d) and the mesophyll conductance (g_m) were used for adjusting estimates to 25 °C. Temperature responses were estimated using the equations described in Harley et al. (1992b). The specific kinetic constants [scaling constant (c), enthalpies of activation (ΔH_a), deactivation (ΔH_d) and entropy (ΔS)] were taken from Sharkey et al. (2007).

Parameters	W_I	W_{II}	W_{III}	W_{IV}	W_V	W_{VI}
Temperature leaf (°C)	32.6 ± 0.2	24.12 ± 0.5	25.2 ± 0.2	26.2 ± 0.2	26.42 ± 0.5	23.5 ± 0.5
Constants for fitting						
K_c (Pa)	61.87	24.73	27.84	31.05	31.82	23.09
K_o (kPa)	21.08	16.12	16.69	17.23	17.35	15.80
Γ^* (Pa)	4.79	3.63	3.77	3.89	3.92	3.56
Constant for adjusting to 25 °C						
R_d (mmol·m^{-2}·s^{-1})	1.601	0.947	1.013	1.078	1.094	0.910
g_m (mmol m^{-2} s^{-1}·Pa^{-1})	1.611	0.943	1.014	1.083	1.100	0.904
Outputs adjusting to 25 °C						
Vcmax (µmol·m^{-2}·s^{-1})	109	118	106	109	101	104
J (µmol·m^{-2}·s^{-1})	201	292	275	259	227	299
TPU (µmol·m^{-2}·s^{-1})	18.6	24.1	23.1	21.2	2.5	25.0

Table 3
Average values of aerosol optical depth (AOD) at 500 nm, the Ångström exponent (AE) at 440–936 nm, air mass and the precipitable water vapor column (in cm) measured using a hand-held sun photometer (MicroTops-II) instrument. The sun photometer measurements were performed at each trial site during the airborne campaigns of 2015–2018.

Year	Site	Flight dates	AOD$_{500\,nn}$	AE$_{440-936nm}$	Air mass	H$_2$O atm (in cm)
2015	Ecija	28/05	0.09	0.84	1.30	1.05
	Carmona	30/05	0.07	0.75	1.28	1.30
2016	Santaella	17/03	0.13	0.69	1.31	1.06
	Santaella	26/04	0.09	0.65	1.27	1.22
2018	Ecija	18/04	0.12	0.61	1.25	0.98
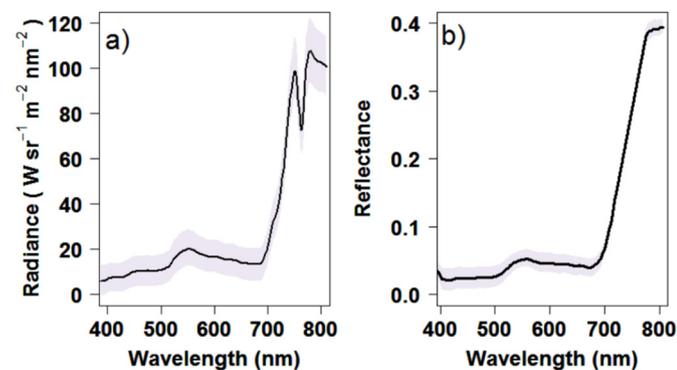
**Fig. 4.** Mean radiance (W·sr^{-1}·m^{-2}·nm^{-1}) (a) and reflectance spectra (b) retrieved from the VNIR hyperspectral camera at the Ecija site in 2018. The black lines correspond to the average spectra of all wheat plots. Shaded areas comprise the ± 1 standard deviation of the average radiance and reflectance profiles.

reflectance distribution function (BRDF) in the VNIR and NIR-100 hyperspectral imagery. Irradiance measurements were interpolated and convoluted to the bandwidth of each sensor. To simulate incoming irradiance, aerosol optical measurements (Table 3) were acquired at flight time with a Microtops II handheld multichannel sunphotometer (Solar Light, Philadelphia, USA) connected to a GPS-12 model (Garmin, Olathe, KS). The aerosol measurements carried out with the sunphotometer instrument at flight-time confirmed the absence of dust mineral, biomass burning (AOD$_{500nm}$ ≤ 0.25 and Ångström exponent (AE) ≥ 0.6, according to Cuevas et al. (2015)) and other extinction aerosols which could affect the reflectance and radiance spectrum during the airborne campaign. A portable weather station (Transmitter PTU30, Vaisala, Helsinki, Finland) was used for simultaneous readings of the relative humidity, temperature and pressure at the time of hyperspectral and thermal acquisitions. Ortho-rectification of hyperspectral imagery was performed following Zarco-Tejada et al. (2016). Sample average radiance and reflectance spectra of wheat plots obtained with the VNIR hyperspectral sensor at the Ecija trial site in 2018 are shown in Fig. 4.

The FLIR SC655 thermal camera used in this study had a resolution of 640 × 480 pixels with a 13.1 mm focal length at 16 bits, providing an angular FOV of 45 × 33.7° and a ground resolution of 25 cm at the flight altitude (Fig. 1d). Thermal imagery was calibrated using ground temperature data collected with a handheld infrared thermometer (LaserSight, Optris, Germany) on each flight date.

2.4. Fluorescence retrieval and calculation of narrow-band indices and CWSI from hyperspectral and thermal imagery

According to the method developed by Camino et al. (2018b), an automatic segmentation based on quartile breaks was applied to the high-resolution hyperspectral imagery for minimizing the effect of the soil background inside wheat plots. The average radiance and reflectance spectra (Fig. 4) were extracted from the high-resolution hyperspectral imagery using the segmented areas, which corresponded with the central region of each wheat plot. Using the same scheme as for the hyperspectral imagery, the watershed segmentation method was applied to high-resolution thermal imagery for separating the vegetation from the soil background.

Solar induced fluorescence (SIF) was quantified from radiance spectra (Fig. 4a) by the *in-filling* method using the Fraunhofer Line Depth (FLD) principle (Plascyk and Gabriel, 1975). The FLD method compares canopy radiance to incoming irradiance at the 760.5 nm atmospheric O_2-A oxygen absorption Fraunhofer Line, as described in Moya et al. (2004) and Meroni et al. (2010). We compared the radiance values L_{in} (L_{762} nm) and L_{out} (L_{750} nm) extracted from the VNIR hyperspectral imagery, to incoming irradiances E_{in} (E_{762} nm) and E_{out} (E_{750} nm) measured at the time of the flights. Reasonable SIF retrieval via the FLD method using broader spectral bandwidths (i.e., 5–7 nm FWHM) has been demonstrated in a simulation study (Damm et al., 2011) and experimentally (Zarco-Tejada et al., 2012, 2016; Damm et al., 2015; Hernández-Clemente et al., 2017). The configuration of the hyperspectral imager during the airborne campaigns carried out in this study (1.85 nm sampling interval, 6.4 nm bandwidths and SNR of 300:1

with spatial binning) is comparable to that of Zarco-Tejada et al. (2012), and observations with the Airborne Prism EXperiment (APEX) sensor in Damm et al. (2015). In addition, NDVI and the pigment-specific simple ratio chlorophyll b index (PSSR$_b$) proposed by Blackburn (1998) were calculated from the average reflectance values for each experimental plot (Fig. 4b).

The Crop Water Stress Index (CWSI) was calculated from the thermal imagery according to the methodology proposed by Idso et al. (1981, Eq. 1). For the assessment of CWSI, the average canopy temperature (Tc) retrieved from the top of the wheat canopy at sunlit conditions and the air temperature (Ta) registered at the flight time were used.

$$CWSI = \frac{(Tc - Ta) - (Tc - Ta)_{LL}}{(Tc - Ta)_{UL} - (Tc - Ta)_{LL}} \qquad (1)$$

(Tc−Ta)$_{LL}$ represents the canopy-air temperature differential of a canopy transpiring at the maximum rate, and (Tc−Ta)$_{UL}$ represents this temperature differential when transpiration is completely halted. The Non-Water-Stress-Baseline (NWSB) was used to derive (Tc−Ta)$_{LL}$, defined as the relationship between the Tc−Ta of a well-irrigated wheat plot at a given vapor pressure deficit (VPD). The NWSB used in this study (Tc-Ta = 3.38−3.25·VPD) was obtained by Idso (1982), while the upper limit was calculated according to the methodology proposed by Idso et al. (1981).

2.5. Modelling methods

Vcmax, standardized to a reference temperature at 25 °C (hereinafter referred to Vcmax), was estimated by inversion of the SCOPE model v1.70 (van der Tol et al., 2009a) using biophysical parameter retrievals and SIF quantification for each wheat plot. SCOPE is a vertical (1-D) integrated radiative transfer and energy balance model.

SCOPE models the relationship between chlorophyll fluorescence and photosynthesis at the leaf level as a function of environmental conditions (van der Tol et al., 2009b). Photosynthesis and chlorophyll fluorescence simulations are carried out in SCOPE with meteorological forcing inputs (incoming shortwave and long-wave radiation, air temperature, humidity, wind speed and CO_2 concentration) and four kinds of parameters: i) leaf parameters including leaf mesophyll structure (N-struct), leaf chlorophyll content (C_{ab}), dry matter content (C_m), leaf equivalent water thickness (C_w), senescent material (C_s) and anthocyanins (C_{ant}); ii) vegetation structural parameters, including the leaf area index (LAI), leaf angle distribution, leaf size and canopy height (h_c); iii) optical parameters, including vegetation emissivity and soil reflectance in the visible, near infrared and thermal bands; and iv) physiological parameters, including stomatal conductance (m) and maximum carboxylation capacity. A summary of the relevant SCOPE inputs for this study is given in Table 4.

The canopy geometry effects on the outgoing spectrum and on the heterogeneity of net radiation are treated stochastically with 60 elementary layers, with a maximum LAI of 0.1 each, 13 discrete leaf zenith inclinations and 36 leaf azimuth classes for shaded and sunlit leaves. The fluorescence contributions from individual leaves are integrated over the canopy layer to calculate top of canopy (TOC) fluorescence in the viewing direction of the hyperspectral sensor based on absorbed fluxes over the photosynthetic active radiation (PAR) region (400–700 nm). The chlorophyll fluorescence at leaf level is computed as a product of the FvCB photosynthesis model, stomatal resistance (Cowan, 1978), the Ball–Berry stomatal conductance model (Ball et al., 1987), the coupled photosynthesis-stomatal model (Collatz et al., 1991), and the emission of chlorophyll fluorescence. The SCOPE model combines the Collatz et al. (1991) model and the Farquhar et al. (1980) photosynthesis model for retrieving the Vcmax, taking into account the stomatal conductance and assimilation rate. For further details see van der Tol et al. (2009b) and van der Tol et al. (2014).

2.5.1. Ancillary climatic data

The meteorological inputs required for SCOPE simulations were extracted from ERA-Interim atmospheric reanalysis data (Dee et al., 2011) produced by the European Centre for Medium-Range Weather Forecasts (ECMWF). The ERA-Interim is the latest global atmospheric reanalysis produced by the ECMWF (http://www.ecmwf.int). Surface parameters extracted from 3-hourly time step ERA-Interim reanalysis included 2-meter air temperature, air pressure, water vapor pressure, incoming shortwave and long-wave downward radiation, and 10-meter wind speeds. The data from ERA-Interim atmospheric reanalysis was spatially interpolated from their native spatial grid (0.75° by 0.75°) to a finer 0.25° by 0.25° resolution using nearest-neighbour resampling. To assess the meteorological variables retrieved from ERA-Interim atmospheric reanalysis, data were compared with observations from the nearest meteorological stations in the regional agro-climatic network (Consejería de Agricultura y Pesca, Junta de Andalucía). Errors associated with convective processes at surface level were reduced using wind speed at 2 m from this network.

2.5.2. Leaf biophysical and structural parameters

The leaf and canopy parameters needed for SCOPE simulations were estimated using a multi-step PROSPECT-SAILH model inversion scheme from reflectance in the 400–1700 nm spectral region. A look-up table (LUT) of 200,000 simulations was built to minimize the *ill-posed inversion* problem (Combal et al., 2003; Li and Wang, 2011; Yebra and Chuvieco, 2009). The range of variation for C_{ab} was determined based on prior field information. The main input parameters were calculated using specific spectral ranges (Table 4) where the biophysical parameters are known to have the greatest influence on reflectance and transmittance spectra. The iterative-optimization numerical (I-optN) approach was used to invert the PROSPECT-SAILH model for the estimation of leaf traits and canopy parameters from reflectance across the observed spectrum. The I-optN method estimates the set of parameters, symbolized by the vector θ = [LADF, *LAI, N, C_{ab}, C_m, C_w*] which minimizes Δ^2 (Eq. (2)). The method calculates the root mean square error (RMSE) between the simulated reflectance and the hyperspectral image reflectance by successive input parameter iteration.

$$\Delta^2 = \sum_n [\rho_{\lambda,obs} - \rho_{\lambda,sim}]^2 \qquad (2)$$

Where $\rho_{\lambda,obs}$ is the image (canopy level) spectral reflectance, and $\rho_{\lambda,sim}$ is the modeled canopy spectral reflectance with a set of parameters defined in the LUT for each wavelength n. The procedure was conducted in several steps: 1) a leaf angle distribution function (LADF) was estimated over the VNIR and SWIR spectral range (400–1750 nm) with variables C_{ab}, C_w and C_m. LADF was first retrieved by model inversion, given its key role in canopy structure; 2) the mesophyll structural parameter (N-struct) and the leaf area index (LAI) were simultaneously determined over the range 960–1300 nm using the LADF from step 1, and variable C_{ab}, C_w and C_m inputs; 3) C_{ab} was then calculated using reflectances in the 455–690 nm range, where chlorophyll *a*bsorption has the strongest effect, with fixed LADF, LAI and N estimated in previous steps; 4) Finally, C_m and C_w were estimated over 900–1700 nm, where dry and water matter have the largest absorption effects (Baret and Fourty, 1997; Feret et al., 2008; Fourty et al., 1996; Jacquemoud et al., 2009, 1996), fixing C_{ab}, LADF, LAI and N obtained previously.

2.5.3. SCOPE iterative-optimization for LIDF$_s$ and R$_{in}$ parameters

After meteorological, leaf, and canopy parameters had been obtained, the SCOPE model was run using an I-optN approach with a LUT table of 27,500 simulations for optimizing the LADF and the broadband incoming shortwave radiation (R$_{in}$). The LADF retrievals derived from PROSPECT-SAILH were optimized with SCOPE iterative-optimization using the radiance spectrum, varying the leaf inclination angle distribution function (LIDF) parameters. The LIDF$_a$ and LIDF$_b$ parameters

Table 4
Range of the PROSPECT-SAILH and SCOPE parameters used in this study.

Parameters	Definition	Unit	Range	Step
PROSPECT				
Leaf biophysical				
N-struct	Leaf mesophyll structure parameter	[−]	1.25–1.85	0.1
C_{ab}	Chlorophyll a + b content	µg·cm^{-2}	10–70	0.5
C_w	Equivalent water thickness	g·cm^{-2}	0.001–0.05	0. 0005
C_m	Dry matter content	g·cm^{-2}	0.001–0.05	0. 0005
C_s	Senescence factor	[−]	0	…
FLUSPECT (integrated into SCOPE model)				
C_{ant}	Anthocyanin content	µg·cm^{-2}	3,5,10	…
SAILH				
Canopy				
LAI	Leaf area index	m^2·m^{-2}	2–5	0.1
LADF	Leaf inclination distribution function	[−]	1,2,3 and 4[a]	…
TV	Solar zenith angle	deg	45,60,85	5
Ph_i	Viewing zenith angle	deg	0	…
PSR	Relative azimuth angle	deg	0	…
S_l	Hot-spot parameter	[−]	0[d]	…
SCOPE				
Leaf biochemistry				
Vcmax	Maximum carboxylation capacity at 25 °C	µmol·m^{-1}·s^{-1}	0–260	10
m	Ball-Berry stomatal conductance	[−]	8	…
Rdparam	Parameter for dark respiration	[−]	0.015	…
K_v	Extinction coefficient for vertical Vcmax profile	[−]	0.64	…
K_c	Cowan's water use efficiency	[−]	700	…
ρ(thermal)	Leaf thermal reflectance	[−]	0.01	…
τ(thermal)	Leaf thermal transmittance	[−]	0.01	…
$ρ_s$(thermal)	Soil thermal reflectance	[−]	0.06	…
Stressfactor	Stress multiplier for Vcmax	[−]	1	…
kNPQs	Rate thermal dissipation	[−]	0	…
qLs	Fraction active photosystems	[−]	1	…
fqe	Fraction of photons partitioned to PSII	[−]	0.02	…
Canopy				
l_w	Leaf width	−	0.1	…
LIDF$_a$	Leaf inclination distribution of leaves	[−]	−1–1	0.05
LIDF$_b$	Variation in leaf inclination	[−]	−1–1	0.05
hc	Canopy height	m	1.2	…
Micrometeorological				
p	Air pressure	hPa	988–997[b]	…
u	Wind speed	m^{-1}	2.2–2.8[c]	…
Oa	O$_2$ concentration in the air	per mille	209	…
ea	Atmospheric vapor pressure	hPa	15	…
Ca	CO$_2$ concentration in the air	ppm	392.2	…
Ta	Air temperature	°C	18–25[b]	…
R_{in}	Incoming shortwave radiation	W·m^{-2}	500–950[b]	…
R_{li}	Incoming longwave radiation	W·m^{-2}	70–150[b]	…

[a] Canopy types proposed to define LADF: planophile (1), erectophile (2), plagiophile (3) and spherical (4).
[b] Meteorological variables retrieved from hourly ERA-Interim reanalysis dataset for each trial sites.
[c] Wind speed at 2-meter from a weather station located close to each trial sites.
[d] Leaves were under sunlit conditions without shadowing effects on the bidirectional reflectance.

mathematically describe the LAD function estimated using PROSP-ECT-SAILH inversions, where LIDF$_a$ determines the average leaf inclination and LIDF$_b$ describes the variation in leaf inclination, controlling the distribution's bimodality.

The I-optN method minimizes a cost function (Eq. (3)) to estimate the set of parameters symbolized by the vector θ = [R$_{in}$, LIDF$_a$, LIDF$_b$]. In this step, the I-optN method was based on the calculation of the RMSE between the *at-sensor* canopy spectral radiance and the SCOPE-simulated spectra by successive input parameter iterations over the spectral region used for the SIF retrievals (740–780 nm).

$$\Delta^2 = \sum_n [L_{\lambda,obs} - L_{\lambda,sim}]^2 \tag{3}$$

Where L$_{\lambda,obs}$ is the measured canopy spectral radiance, and L$_{\lambda,sim}$ is the canopy spectral radiance modeled by SCOPE with the set of parameters defined in the LUT for a given wavelength n. The LUT was built varying R$_{in}$ and LIDF$_s$, but keeping the Vcmax constant at 80 µmol·m^{-2}·s^{-1} and the remaining default values fixed, as shown in

Table 1. R$_{in}$ varied 100 W·m^{-2} with a step of 5–10 W·m^{-2} from the incoming shortwave radiation from the ERA-Interim reanalysis for each trial site. The leaf inclination distribution factors (LIDF$_a$ and LIDF$_b$) varied according to the LADF obtained from PROSPECT-SAILH inversions, using a total of 500 variations. Among the canopy structural variables, LIDF$_a$, representing the inclination distribution of leaves, had the greatest effect on SIF variability. In fact, LIDF$_a$ had a large influence on modeled reflectance with a contribution of over 20% of the variation between 720 and 1150 nm, while the LAI parameter governed over ≥50% of variation in reflectance at wavelengths longer than 1400 nm. The remaining structural inputs used in SCOPE (leaf width, LIDF$_b$, and canopy height) had a marginal impact on the modeled reflectance (Verrelst et al., 2015). Recent studies (Koffi et al., 2015; Verrelst et al., 2016, 2015) have demonstrated the importance of R$_{in}$, since the fluorescence spectrum is proportional to the absorbed PAR.
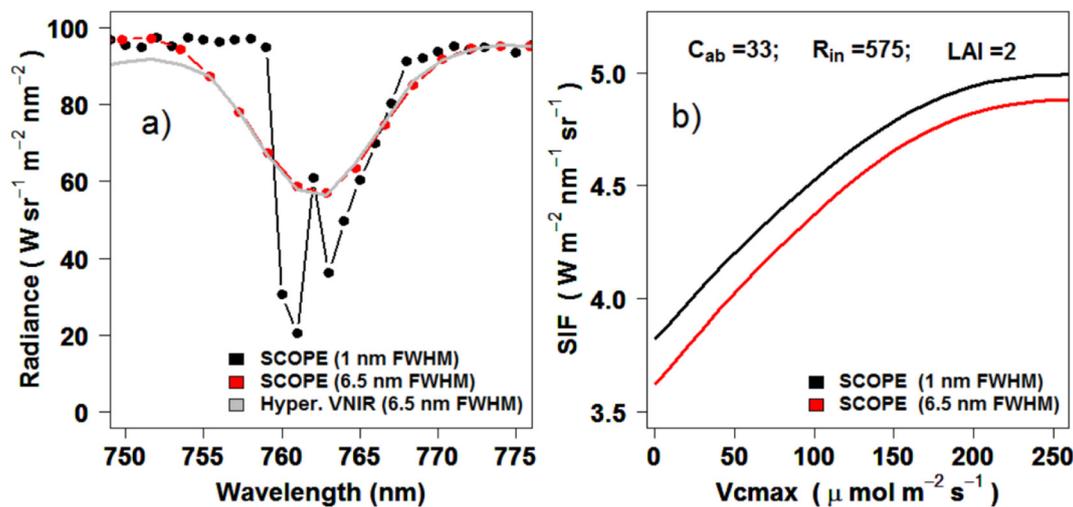
Fig. 5. Radiance spectra obtained by the VNIR hyperspectral sensor (in grey), the radiance simulated by SCOPE model at 1 nm (in black) and the convoluted SCOPE-simulated radiance using Whittaker-Shannon interpolation and moving average filters (in red) (a). For the same wheat plot, the SCOPE-simulated SIF (black line) and the SIF obtained after convolution (red line) are shown as a function of Vcmax ($\mu mol \cdot m^{-2} \cdot s^{-1}$) (b) for simulations with C_{ab} = 33 $\mu g \cdot cm^{-2}$, LAI = 2 and R_{in} = 575 $W \cdot m^{-2}$. (For interpretation of the references to color in this figure legend, the reader is referred to the web version of this article.)

2.5.4. Vcmax estimation from SCOPE model inversion

Once the leaf, canopy and meteorological parameters were obtained following the I-optN approaches using the PROSPECT-SAILH and SCOPE simulations, the relationships between Vcmax and canopy fluorescence (Vcmax = f(SIF); Fig. 5b) were established for all wheat plots. For this purpose, the SCOPE model was run in forward mode with the Vcmax range set to 0–260 $\mu mol \cdot m^{-2} \cdot s^{-1}$, divided into 27 intervals. As an additional step, the simulated radiance spectra from SCOPE at 1 nm resolution in the 640–800 spectral windows was convoluted using the Whittaker-Shannon interpolation, as described in Butzer et al. (2011). Fig. 5a shows the comparison between the radiance retrieved with the VNIR hyperspectral sensor, the original radiance simulated by SCOPE at 1 nm, and the simulated SCOPE radiance spectra convoluted to match the airborne hyperspectral data. The spectral convolution of the radiance simulated by SCOPE was critical to match the broader resolution of the hyperspectral imager, and therefore to obtain comparable SIF values. Fig. 5b shows the effect of the convoluted radiance signal when applied to the SCOPE simulations, observing the relationship between SIF and Vcmax.

3. Results

3.1. Nutrient and water-stress variability in rainfed and irrigated study sites

Field-based leaf physiological measurements (net assimilation, N concentration and water potential), Vcmax estimated by SCOPE inversions, C_{ab} estimated by PROSPECT-SAILH inversions, and CWSI for the entire experiment comprising rainfed and irrigated plots are shown in Fig. 6. There were large differences in the crop photosynthesis, water and nitrogen status between water regimes. As expected, irrigated plots had better water and nutritional status compared to rainfed plots overall. Irrigated plots had higher assimilation rates, N concentrations, Vcmax, and C_{ab} (Fig. 6a, b, d and e) than rainfed plots. ANOVA analysis confirmed statistically significant differences between the means of the two water stress regimes for all field physiological measurements (all p-values $\leq$ 0.0036).

There was a significant correlation between CWSI and water potential in rainfed plots (r^2 = 0.30, p-value = 0.7e-4), although the correlation was stronger for irrigated plots (r^2 = 0.72, p-value = 1.7e-5). The high variability in N concentration for both treatments (Fig. 6b) suggests that rainfed plots were also affected by N deficit. Assimilation rate was significantly correlated with the N concentration (r^2 = 0.51

and 0.56 for irrigated and rainfed, respectively) indicating that the N concentration also affected the photosynthetic capacity in both water regimes.

3.2. Effects of the biochemical and environmental parameters on SIF and Vcmax estimation

The sensitivity of the convoluted radiance signal simulated with SCOPE to chlorophyll content, LAI and the broadband incoming shortwave radiation are shown in Fig. 7. Variation in Cab had a relatively small effect on radiance at the spectral region typically used to quantify chlorophyll fluorescence (750–775 nm), particularly as compared to LAI and R_{in} (Fig. 7b and c). In general, for the same value of C_{ab}, the radiance significantly increased with the increase of LAI and R_{in} in the O_2-A region. However, large differences were observed as a function of R_{in} variation, reaching > 30 $W \cdot sr^{-1} \cdot m^{-2} \cdot nm^{-2}$. These results showed that R_{in} was a key micrometeorological variable in driving SIF variability simulated by the SCOPE model.

Fig. 8 shows the relationship between SCOPE-simulated SIF and Vcmax, as a function of LAI, C_{ab} and R_{in}. At constant radiation (R_{in} = 800 $W \cdot m^{-2}$) and LAI (2), fluorescence increased with increasing values of C_{ab} and Vcmax. The largest increase in the SIF retrievals occurred for Vcmax between 10 and 60 $\mu mol \cdot m^{-2} \cdot s^{-1}$. For larger Vcmax values ($\geq$ 150 $\mu mol \cdot m^{-2} \cdot s^{-1}$), SIF retrievals remained steady, with a tendency to increase with C_{ab}.

At constant C_{ab}, there were dramatic changes in the relationship between simulated SIF and Vcmax with increased with LAI and R_{in} (Fig. 9b and c). SIF significantly increased with LAI, nearly doubling with an increase in LAI from 1 to 5 (Fig. 8b). Unsurprisingly, SIF increased proportionally to R_{in} (Fig. 8c).

3.3. Validation of Vcmax estimated by SCOPE using leaf photosynthesis measurements

The relationship between the SCOPE-estimated Vcmax and the field-measured Vcmax is shown in Fig. 9a. There was an almost 1:1 linear relationship (r^2 = 0.77; p-value $\leq$ 2.2e-16 and RMSE = 2.6 $\mu mol \cdot m^{-2} \cdot s^{-1}$) between measured and estimated Vcmax, using the FvCB approach on the six wheat varieties from the airborne campaign in 2018. The relationships between net photosynthetic rate and both measured and simulated Vcmax also displayed a significant relationship for both types of Vcmax estimates (all $r^2 \geq$ 0.68; p-value
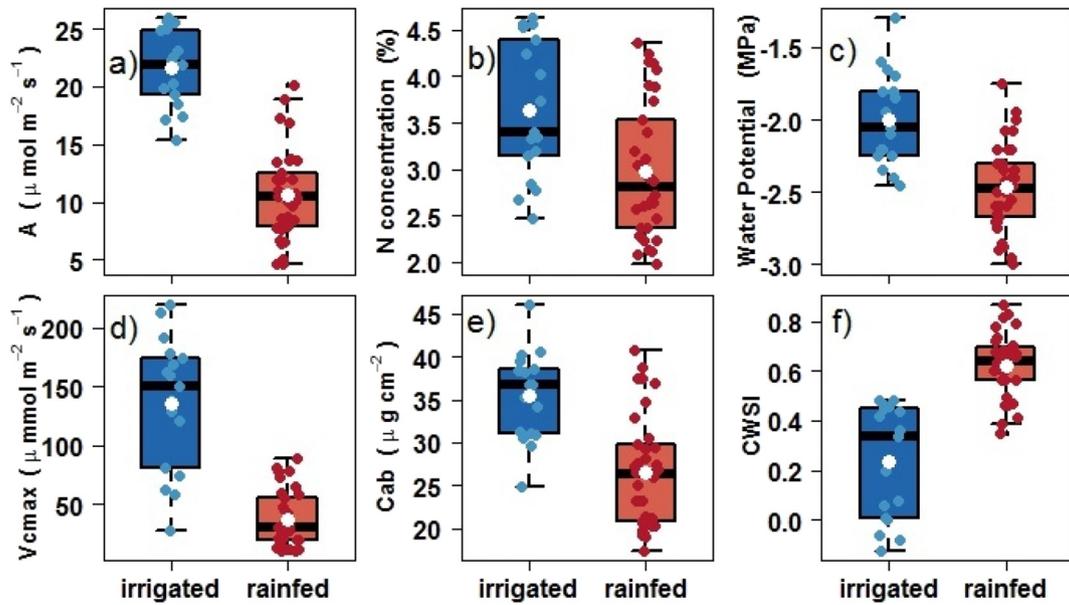
Fig. 6. Leaf- and canopy-level physiological data acquired in plots under rainfed (red) and irrigated (blue) conditions: a) assimilation rate ($\mu mol \cdot m^{-2} \cdot s^{-1}$); b) leaf N concentration (%); c) water potential (MPa); d) Vcmax estimated by SCOPE ($\mu mol \cdot m^{-2} \cdot s^{-1}$); e) chlorophyll content estimated by PROSPECT-SAILH ($\mu g \cdot cm^{-2}$); and f) CWSI calculated from high-resolution thermal imagery. In the box plots, the horizontal line represents the median, and the top and bottom are the 75th and 25th quartiles, respectively. The whiskers represent the upper and lower range. Average values shown with a white point over the box plot. (For interpretation of the references to color in this figure legend, the reader is referred to the web version of this article.)

≤ 0.005) (Fig. 9b).

The relationship between Vcmax simulated by SCOPE model inversion and SIF quantified from the hyperspectral imagery at the different trial sites yielded a significant non-linear relationship ($r^2 = 0.84$; p-value $\leq 2.2e$-16; Fig. 11). Irrigated plots had high SIF values ($\geq 4.92 \, W \cdot sr^{-1} \cdot m^{-2} \cdot nm^{-2}$) that were related to large values of Vcmax, mainly over $100 \, \mu mol \cdot m^{-2} \cdot s^{-1}$. Under the severe water stress conditions in most rainfed plots, Vcmax was lower than $90 \, \mu mol \cdot m^{-2} \cdot s^{-1}$. However, for some rainfed plots (Ecija 2018), which were in an early growth stage and under moderate water stress, Vcmax and SIF retrievals were larger than $90 \, \mu mol \cdot m^{-2} \cdot s^{-1}$ and $5 \, W \cdot sr^{-1} \cdot m^{-2} \cdot nm^{-2}$ for

Vcmax and SIF, respectively.

3.4. Relationships between Vcmax and net assimilation under irrigation and rainfed conditions

The relationships between net assimilation and SCOPE-estimated Vcmax, CWSI, leaf C_{ab}, and NDVI are shown in Fig. 11 and Fig. 12 for each water regime. The SCOPE-estimated Vcmax was significantly correlated with the assimilation rate ($r^2 = 0.50$, p-value = 2.91e-6) under rainfed conditions. This relationship was stronger under irrigated conditions ($r^2 = 0.65$, p-value = 9.31e-5). The slightly weaker
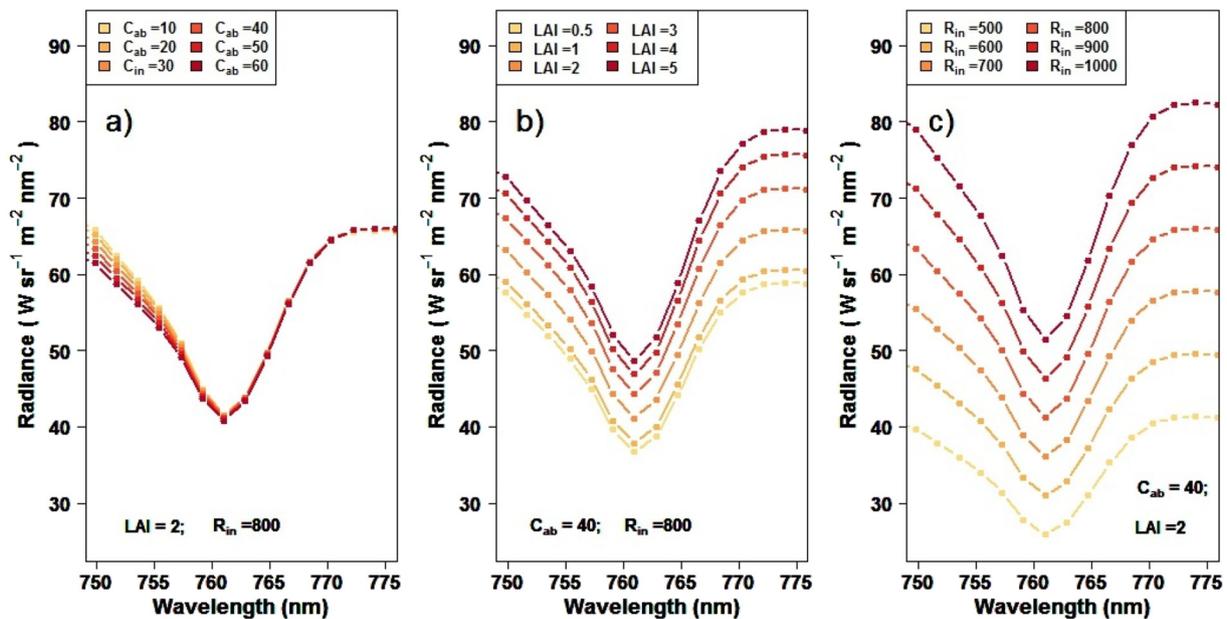
Fig. 7. Sensitivity of SCOPE radiance profiles convoluted to match the FWHM of the hyperspectral imager used in the study, as a function of chlorophyll content (C_{ab}) in $\mu g \cdot cm^{-2}$ (a), leaf area index (LAI) (b) and the broadband incoming shortwave radiation (R_{in}) in $W \cdot m^{-2}$ (c) for Vcmax = $80 \, \mu mol \cdot m^{-2} \cdot s^{-1}$. CO_2 and O_2 concentration at the interface of the canopy were set to 382.17 ppm and 200×103 ppm, respectively.
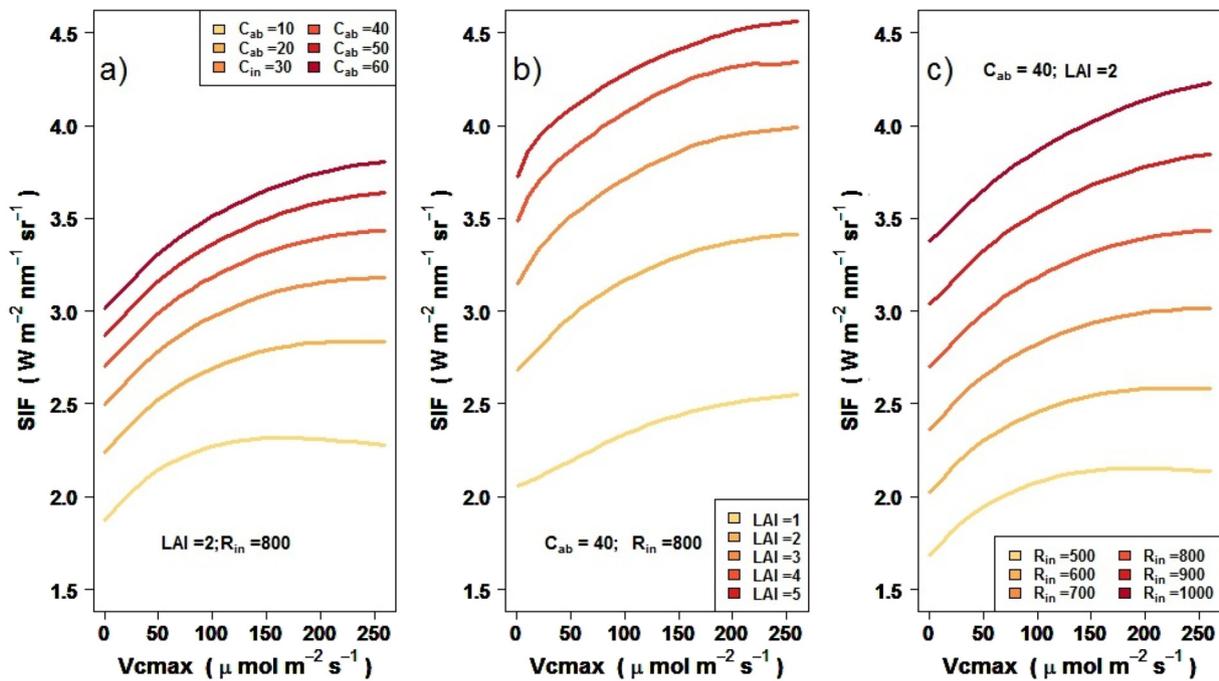
Fig. 8. Relationships between SIF estimated from SCOPE radiance simulations and Vcmax (μmol·m^{-2}·s^{-1}) as a function of chlorophyll content (C_{ab}) in μg·cm^{-2} (a), LAI (b) and the broadband incoming shortwave radiation (R_{in}) in W·m^{-2} (c).

correlation obtained in rainfed plots could be associated with nutrient and water limitations, as well as an increased influence of background effects under stress conditions. In this context, variation in Vcmax was reduced and values were smaller ($< 90\ \mu$mol·m^{-2}·s^{-1}), relative to irrigated conditions.

Net assimilation was significantly related to C_{ab} ($r^2 = 0.56$; p-value = 3.93e-7), NDVI ($r^2 = 0.46$; p-value = 1.19e-5) and PSSR$_b$ ($r^2 = 0.56$; p-value = 4.21e-7) under rainfed conditions (Fig. 12b, c and d). Under rainfed conditions, chlorophyll indicators (C_{ab} and PSSR$_b$) had better correspondence to net assimilation than remote sensing estimates of Vcmax ($r^2 = 0.50$). By contrast, the relationship between the assimilation rate and the thermal-based CWSI (Fig. 12a) was weak ($r^2 = 0.14$, p-value < 0.03), suggesting that the chronic water-stress may have resulted in an associated nutrient deficiency that

limited assimilation rates. Indeed, net assimilation under rainfed conditions was more related to nitrogen and pigment indicators rather than to CWSI. Furthermore, after the supplemental irrigation in the Carmona plots in 2015, photosynthetic rates remained low despite partially recovered water status. For these plots, CWSI reached values close to 0.4, while assimilation rates were maintained below 15 μmol·m^{-2}·s^{-1}.

Under well-irrigated conditions, the relationships between net assimilation and C_{ab}, NDVI and PSSR$_b$ showed weak, nonsignificant relationships ($r^2 < 0.13$; p-value = 0.83 for leaf C_{ab} content; p-value = 0.41 for PSSR$_b$; p-value = 0.15 for NDVI, Fig. 12). It is likely that these relationships exhibited scaling problems due to saturation effects associated with high canopy densities in irrigated plots. By contrast, the relationship between net assimilation and CWSI was strongly correlated for irrigated plots ($r^2 = 0.73$, p-value = 1.30e-5).
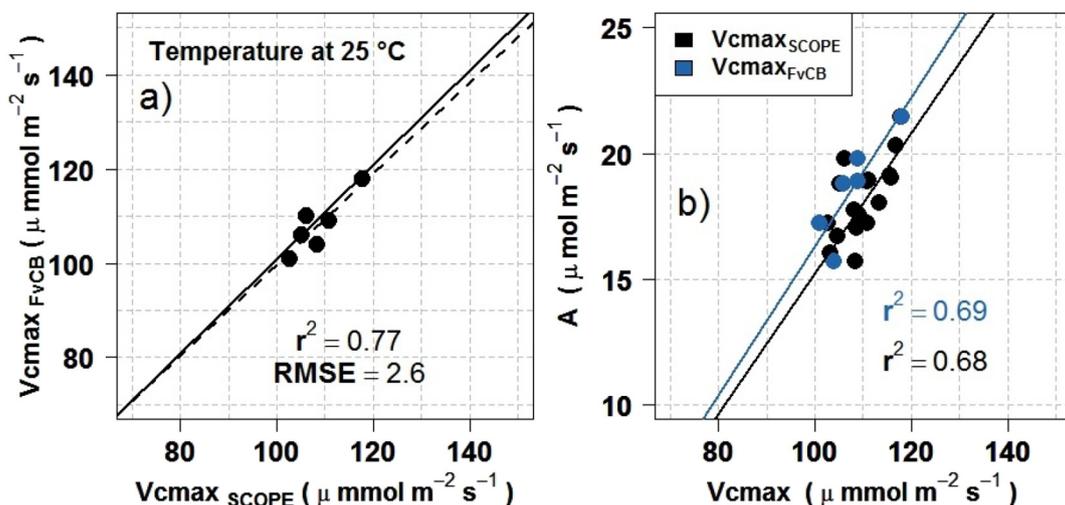
Fig. 9. a) Relationship between carboxylation maximum capacity (Vcmax; μmol·m^{-2}·s^{-1}) retrieved from the hyperspectral image through the SCOPE model inversion vs. field measured Vcmax through Farquhar–von Caemmerer–Berry (FvCB) model using the curve A/C$_i$ (wheat Ecija plots, 2018). The black line is the fit line and the dashed line is the one-to-one line; b) relationships between the average net assimilation (A; μmol·m^{-2}·s^{-1}) measured using the photosynthesis chamber at flight time and the simulated Vcmax (in black dots) and the Vcmax calculated from FvCB model (in blue dots). (For interpretation of the references to color in this figure legend, the reader is referred to the web version of this article.)
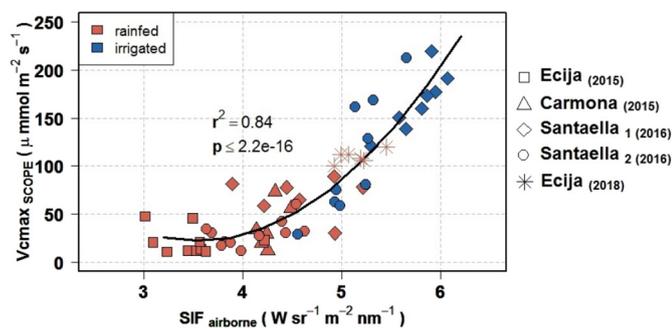
Fig. 10. Relationship between carboxylation maximum capacity (Vcmax, $\mu mol \cdot m^{-2} \cdot s^{-1}$) estimated by hyperspectral imagery through SCOPE model inversion and SIF quantified from the hyperspectral imagery, displaying rainfed (red) and irrigated (blue) conditions. Each symbol corresponds with a single plot measurement. (For interpretation of the references to color in this figure legend, the reader is referred to the web version of this article.)

The estimation of Vcmax as a function of SIF retrievals enabled the calculation of the spatial distribution of Vcmax and the net assimilation in the wheat experimental plots (Fig. 13). These pixel-level estimates of Vcmax and assimilation for rainfed and irrigated wheat varieties were retrieved using the modelled regression between SIF and Vcmax shown in Fig. 10.

4. Discussion

Several studies have shown the utility of remotely-sensed SIF as an indicator of the photosynthetic activity at across spatial resolutions (Meroni et al., 2009; Porcar-Castell et al., 2014; Rascher et al., 2015). SIF retrieved from satellite imagery has improved estimations of gross primary productivity at ecosystem to global scales (Frankenberg et al., 2011; Guanter et al., 2014; Smith et al., 2018). However, SIF-GPP relationships require appropriate modelling methods to compensate for structural effects of vegetation canopies (Levula et al., 2019), spatial and temporal scales (Hu et al., 2018), seasonal changes in photosynthetic pigments (Campbell et al., 2018), environmental conditions (Verma et al., 2017) and other confounding factors. In this regard, He et al. (2017) showed that the sun-satellite view observation geometry could produce unwanted SIF variations, affecting the accuracy of GPP. Due to its close link to photosynthetic activity, SIF also has great potential for use in precision agriculture and plant breeding programs. At both global (satellite) and local (airborne and drone) scales, remote estimation of the maximum rate of carboxylation, Vcmax is thought to be a suitable proxy for photosynthesis. Zhang et al. (2014) demonstrated that estimation of Vcmax from space-based SIF retrievals combined with SCOPE simulations in corn and soybean crops was feasible. Nevertheless, further work was needed to understand if these methods are applicable to remote sensing instruments readily available in the context of routine precision agriculture operations and in plant breeding programs. In particular, it is necessary to test whether SIF and Vcmax retrievals are feasible with the technical constraints of the spectral resolution available for operational and commercial remote sensing work, the high spatial resolution required, and the general aim of detecting subtle physiological changes across varieties and under water and nutrient stress levels.

The work presented here demonstrates that the Vcmax estimated from airborne hyperspectral imagery through SCOPE model inversion was able to detect physiological changes induced by differing irrigation regimes and crop varieties. The relationships between net photosynthetic rates and both measured Vcmax and simulated Vcmax (Fig. 9b) at the Ecija site were significantly correlated ($r^2 \geq 0.68$ and p-value ≤ 0.005). The sample size used in the validation of SCOPE-simulated Vcmax was low due to the time-consuming nature of obtaining CO_2 response curves. Nevertheless, a larger dataset ($n > 50$) was used
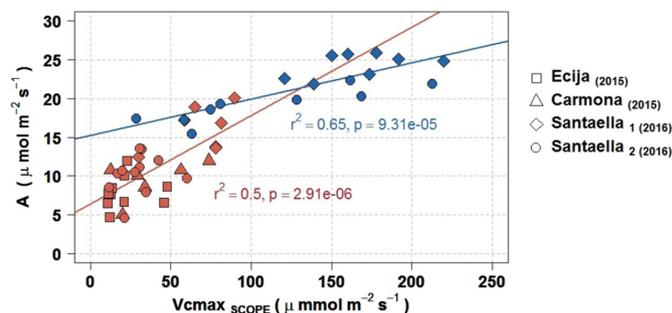
Fig. 11. Relationships between average assimilation (A; $\mu mol \cdot m^{-2} \cdot s^{-1}$) measured in leaves and Vcmax ($\mu mol \cdot m^{-2} \cdot s^{-1}$) estimated by hyperspectral imagery through SCOPE model inversion under rainfed (red; $n = 33$) and irrigated (blue, $n = 18$) conditions. The average net assimilation per plot was obtained using two leaves from the top of the canopy and a portable photosynthesis chamber. (For interpretation of the references to color in this figure legend, the reader is referred to the web version of this article.)

to demonstrate the relationship between Vcmax retrieved from SCOPE and plant physiological traits (Fig. 11 and Fig. 12). It demonstrates that Vcmax estimates are related to the physiological changes associated to water status. Issues related to the coarser spectral resolution of hyperspectral instruments used in precision agriculture and plant breeding programs were evaluated with respect to SIF retrieval, and its impact on Vcmax estimation, as validated by field measurements of plant traits and net assimilation. In particular, the small plot sizes normally used by plant breeders during their wheat selection trials may limit the accuracy of remotely-sensed SIF. The planting-row designs with 25-cm row spacing used in this study could affect the retrievals of narrow-band and high-resolution hyperspectral (25 cm) and thermal (20 cm) imagery. When the plots are too small, soil and background effects may contaminate the signal due to the mixing of the soil and vegetation reflectance. Therefore, segmentation algorithms should be implemented to reduce soil background effects on estimates of plant physiological traits at canopy level, especially in early growth stages where these effects could significantly reduce the accuracy of retrievals. This issue is especially relevant for coarse-resolution sensors such as the SWIR camera (70 cm) and the thermal sensors. Spatial resolution issues should be considered during the experimental design in breeding programs where the remote sensing sensors are expected to be used.

The SCOPE-simulated radiance data which was convoluted to match the spectral resolution of the airborne hyperspectral imager used in our study was critical for obtaining SIF and Vcmax parameters within expected ranges. Analysis confirmed that the canopy structure and the incoming shortwave radiation were the main driving variables for modeled SIF emissions (Verrelst et al., 2015, 2016). In particular, R_{in} had a dominant influence on SIF, as expected based on the pivotal role of PAR load on fluorescence emission. As explained in Van der Tol et al. (2014), PAR and Vcmax are the main contributors to the fluorescence yield in SCOPE. The effects of chlorophyll content, LAI and R_{in} on the relationship between SIF and Vcmax were also included in the sensitivity analysis reported in our manuscript, showing the large impact of C_{ab} on the SIF-Vcmax relationships (Fig. 8a), which is in agreement with Koffi et al. (2015).

Estimates of Vcmax from wheat plot image spectra through SCOPE model inversion were within the ranges reported by other studies for wheat crops (10–219 $\mu mol \cdot m^{-2} \cdot s^{-1}$; Wullschleger, 1993; Silva-Pérez et al., 2017). The relationship between the estimated Vcmax and chlorophyll fluorescence ($r^2 = 0.84$; Fig. 10) differed greatly between irrigated and water-stressed plots. As shown in Fig. 10, the SIF and Vcmax are modulated by water status. In this regard, Zheng et al. (2017) showed that photosynthesis at noon is mainly limited by Vcmax, further indicating that Vcmax may be a suitable proxy for evaluating plant stress levels. For irrigated conditions, the relationship was almost
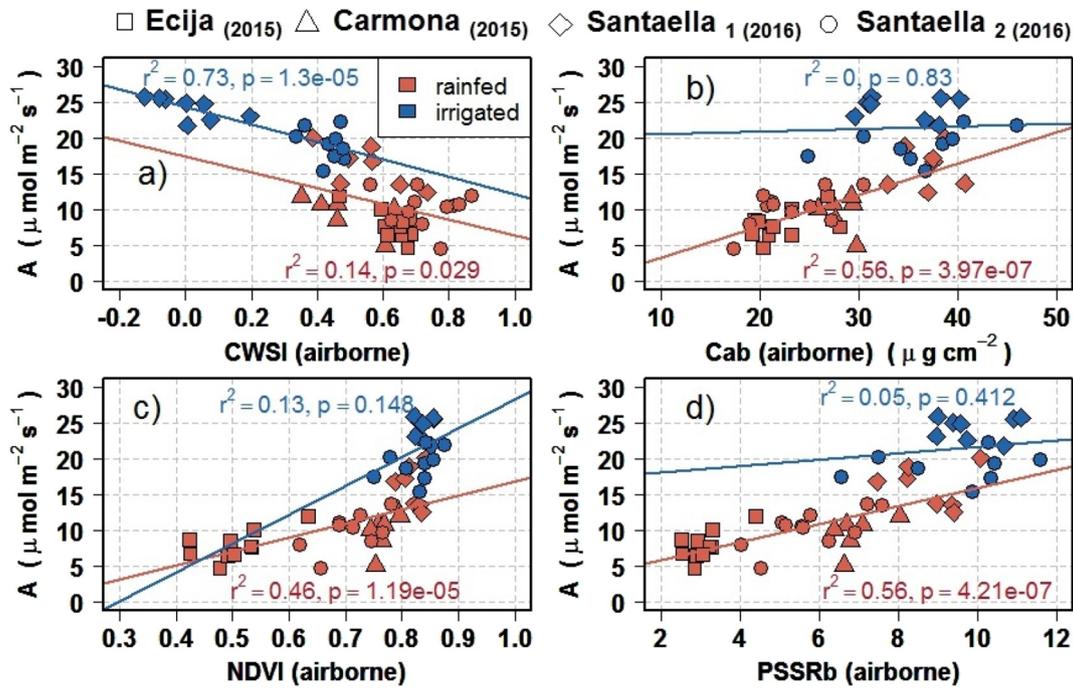
Fig. 12. Relationships between average net assimilation (A, μmol·m^{-2}·s^{-1}) and (a) CWSI, (b) chlorophyll content (C$_{ab}$; μg·cm^{-2}) estimated by PROSPECT-SAILH model inversion, (c) NDVI, and (d) PSSR$_b$ calculated from hyperspectral imagery under rainfed (red points; n = 33) and irrigated (blue points, n = 18) conditions. Average net assimilation per plot was obtained from two leaves at the top of the canopy with a portable photosynthesis chamber. (For interpretation of the references to color in this figure legend, the reader is referred to the web version of this article.)

linear and displayed a steeper slope with larger Vcmax values (≥100 μmol·m^{-2}·s^{-1}). Under water deficit the relationship was weak. As crops reduce stomatal and mesophyll conductance in response to stress, the CO_2 concentration within the chloroplast drops, causing a reduction in the photosynthesis capacity (Vcmax). Under low CO_2 concentrations, plant carboxylation rates are limited by RuBisCo rather than Vcmax (Sharkey et al., 2007). Consequently, under severe water stress, both Vcmax and SIF retrievals were suppressed, which is in agreement with the findings by Zheng et al. (2017).

Due to the intensive field-work required to estimate the relationships between A and Ci, the number of observations used to estimate Vcmax in the field was small. Nevertheless, our data suggests that simulated Vcmax corresponded well with in situ measurements. The results were satisfactory (r^2 = 0.77; p-value ≤2.2e-16 and RMSE = 2.6 μmol·m^{-2}·s^{-1}) despite the limited number of leaf Vcmax samples, suggesting that Vcmax could reasonably be estimated from SCOPE and convoluted SIF retrievals using hyperspectral imaging technology suitable for precision agriculture. Simulated Vcmax yielded
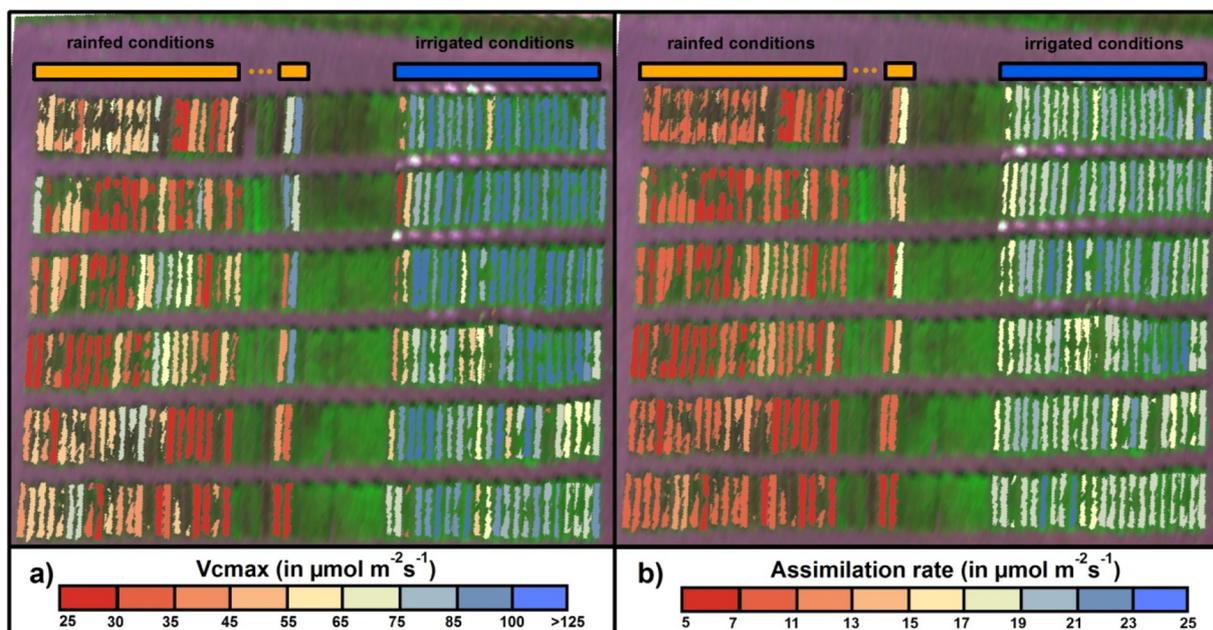
Fig. 13. Maps of Vcmax (μmol·m^{-2}·s^{-1}) (a) and assimilation rate (A; μmol·m^{-2}·s^{-1}) (b) predicted from Vcmax, under irrigated and rainfed conditions at Santaella field site during 2016 airborne campaign.

a significant relationship with assimilation rate at the Ecija site in 2018 under non severe water stress conditions ($r^2 = 0.68$; p-value ≤ 0.005). These results are in accordance with results obtained by Zhang et al. (2014, 2018) in soybean and corn crops. The relationships observed between Vcmax and the net photosynthesis (Fig. 11) supports the hypothesis that airborne-quantified Vcmax is a feasible indicator of crop functioning under contrasting water regimes. Moreover, we showed (Fig. 12) that in the absence of water stress, Vcmax was a stronger predictor of photosynthetic capacity than standard indicators such as C_{ab}, and NDVI and $PSSR_b$. These indicators likely performed poorly due to scaling problems related to the high canopy densities in irrigated plots. As a result, non-significant relationships were also found between net assimilation and these indices (all p-value ≥ 0.15). In dense biomass canopies, the NIR reflectance increases greatly, reducing the sensitivity of the normalized ratios such as NDVI or $PSSR_b$ to plant biochemical content (Thenkabail et al., 2000; Gitelson, 2004).

Under rainfed conditions, i.e. in the presence of water stress, Vcmax, C_{ab} and reflectance indices were related to CO_2 assimilation rate, but thermal CWSI was not. Under water stress, stomatal closure reduces the CO_2 concentration inside the chloroplast, decreasing the photochemical activity and also photo-inhibition processes (Flexas and Medrano, 2002). Thus, leaf photochemistry decreases, resulting in a reduction of the chlorophyll fluorescence and RuBisCo activity. The fact that reflectance-based indicators (C_{ab}, $PSSR_b$, and NDVI) became significantly associated to A, under water stress, suggests that the saturation effects from canopy biomass were not present in rainfed plots. In this study, partial recovery of the water status (as happened in Carmona field in 2015) after sever water stress did not result in elevated assimilation rates. This suggests that instantaneous assessment of water status might not track photosynthetic performance if severe water stress has affected the photosynthetic apparatus.

From an operational perspective, the remote estimation of Vcmax from high-resolution hyperspectral imagery through SCOPE model inversion methods provides a powerful tool to accurately assess crop assimilation rates in large plant breeding programs and in precision agriculture studies. Moreover, its robustness across both irrigated and water-stressed plots was demonstrated when compared against standard reflectance-based remote sensing indicators widely used for crop screening and high-throughput phenotyping.

5. Conclusions

The work presented in this manuscript demonstrates the estimation of maximum rate of carboxylation (Vcmax) using SCOPE model inversion with airborne-quantified SIF from hyperspectral imagery. Estimates suitably tracked photosynthetic rates and clearly distinguished physiological differences in irrigated and rainfed conditions. Under water stress, all plant trait indicators performed similarly (Vcmax, NDVI, Cab and $PSSR_b$) and were well related to assimilation rates. Nevertheless, estimated Vcmax outperformed standard remote sensing indices for the quantification of crop photosynthesis under irrigated conditions (i.e. in the absence of water stress). The methodology demonstrated in this study is directly relevant for high-throughput plant phenotyping and for precision agriculture applications.

Acknowledgements

References

Ball, J.T., Woodrow, I.E., Berry, J.A., 1987. In: Biggins, J. (Ed.), A Model Predicting Stomatal Conductance and its Contribution to the Control of Photosynthesis under Different Environmental Conditions BT - Progress in Photosynthesis Research: Volume 4 Proceedings of the VIIth International Congress on Photosynthesis Providence, Rhode Island, USA, August 10–15, 1986. Springer Netherlands, Dordrecht, pp. 221–224. https://doi.org/10.1007/978-94-017-0519-6_48.

Baret, F., Fourty, T., 1997. Estimation of leaf water content and specific leaf weight from reflectance and transmittance measurements. Agronomie 17, 455–464. https://doi.org/10.1051/agro:19970903.

Blackburn, G.A., 1998. Spectral indices for estimating photosynthetic pigment concentrations: a test using senescent tree leaves. Int. J. Remote Sens. 19, 657–675. https://doi.org/10.1080/014311698215919.

Butzer, P.L., Ferreira, P.J.S.G., Higgins, J.R., Saitoh, S., Schmeisser, G., Stens, R.L., 2011. Interpolation and sampling: E.T. Whittaker, K. Ogura and their followers. J. Fourier Anal. Appl. 17 (2), 320–354. https://doi.org/10.1007/s00041-010-9131-8.

Caemmerer, S. Von, 2000. Biochemical models of leaf photosynthesis. Tech. Plant Sci. 53, 1689–1699. https://doi.org/https://doi.org/10.1017/CBO9781107415324.004.

Caemmerer, S. Von, Farquhar, G.D., 1981. Some relationships between the biochemistry of photosynthesis and the gas exchange of leaves. Planta 153, 376–387. https://doi.org/https://doi.org/10.1007/BF00384257.

Cairns, J.E., Sanchez, C., Vargas, M., Ordoñez, R., Araus, J.L., 2012. Dissecting maize productivity: ideotypes associated with grain yield under drought stress and well-watered conditions. J. Integr. Plant Biol. 54, 1007–1020. https://doi.org/10.1111/j.1744-7909.2012.01156.x.

Camino, C., González-Dugo, V., Hernández, P., Sillero, J.C., Zarco-Tejada, P.J., 2018a. Improved nitrogen retrievals with airborne-derived fluorescence and plant traits quantified from VNIR-SWIR hyperspectral imagery in the context of precision agriculture. Int. J. Appl. Earth Obs. Geoinf. 70, 105–117. https://doi.org/10.1016/j.jag.2018.04.013.

Camino, C., Zarco-Tejada, P.J., Gonzalez-Dugo, V., 2018b. Effects of heterogeneity within tree crowns on airborne-quantified SIF and the CWSI as indicators of water stress in the context of precision agriculture. Remote Sens. 10. https://doi.org/10.3390/rs10040604.

Campbell, P.K., Huemmrich, K.F., Middleton, E.M., Ward, L.A., 2018. Diurnal and Seasonal Variations in Chlorophyll Fluorescence Associated with Photosynthesis at Leaf and Canopy Scales 1–36. https://doi.org/https://doi.org/10.3390/rs11050488.

Carmo-Silva, E., Andralojc, P.J., Scales, J.C., Driever, S.M., Mead, A., Lawson, T., Raines, C.A., Parry, M.A.J., 2017. Phenotyping of field-grown wheat in the UK highlights contribution of light response of photosynthesis and flag leaf longevity to grain yield. J. Exp. Bot. 68, 3473–3486. https://doi.org/10.1093/jxb/erx169.

Chaves, M.M., 1991. Effects of water deficits on carbon assimilation. J. Exp. Bot. 42, 1–16. https://doi.org/10.1093/jxb/42.1.1.

Collatz, G.J., Ball, J.T., Grivet, C., Berry, J.A., 1991. Physiological and environmental regulation of stomatal conductance, photosynthesis and transpiration: a model that includes a laminar boundary layer. Agric. For. Meteorol. 54, 107–136. https://doi.org/10.1016/0168-1923(91)90002-8.

Collatz, G., Ribas-Carbo, M., Berry, J.A., 1992. Coupled photosynthesis-stomatal conductance model for leaves of C4 plants. Aus. J. Plant Physiol. 1 (9), 519–538.

Combal, B., Baret, F., Weiss, M., Trubuil, A., Macé, D., Pragnère, A., Myneni, R., Knyazikhin, Y., Wang, L., 2003. Retrieval of canopy biophysical variables from bi-directional reflectance using prior information to solve the ill-posed inverse problem. Remote Sens. Environ. 84, 1–15. https://doi.org/https://doi.org/10.1016/S0034-4257(02)00035-4.

Cowan, I.R., 1978. In: Preston, R.D., Woolhouse, H.W.B.T.-A. (Eds.), Stomatal Behaviour and Environment. Academic Press, pp. 117–228. https://doi.org/10.1016/S0065-2296(08)60370-5. in B.R. (Eds.).

Croft, H., Chen, J.M., Luo, X., Bartlett, P., Chen, B., Staebler, R.M., 2017. Leaf chlorophyll content as a proxy for leaf photosynthetic capacity. Glob. Chang. Biol. 23, 3513–3524. https://doi.org/10.1111/gcb.13599.

Cuevas, E., Camino, C., Benedetti, A., Basart, S., Terradellas, E., Baldasano, J.M., Morcrette, J.J., Marticorena, B., Goloub, P., Mortier, A., Berjón, A., Hernández, Y., Gil-Ojeda, M., Schulz, M., Berj??n, A., Hern??ndez, Y., Gil-Ojeda, M., Schulz, M., 2015. The MACC-II 2007-2008 reanalysis: atmospheric dust evaluation and characterization over northern Africa and the Middle East. Atmos. Chem. Phys. 15, 3991–4024. https://doi.org/10.5194/acpd-14-27797-2014.

Damm, A., Erler, A., Hillen, W., Meroni, M., Schaepman, M.E., Verhoef, W., Rascher, U., 2011. Modeling the impact of spectral sensor configurations on the FLD retrieval accuracy of sun-induced chlorophyll fluorescence. Remote Sens. Environ. 115, 1882–1892. https://doi.org/10.1016/j.rse.2011.03.011.

Damm, A., Guanter, L., Paul-Limoges, E., van der Tol, C., Hueni, A., Buchmann, N., Eugster, W., Ammann, C., Schaepman, M.E., 2015. Far-red sun-induced chlorophyll fluorescence shows ecosystem-specific relationships to gross primary production: an assessment based on observational and modeling approaches. Remote Sens. Environ. 166, 91–105. https://doi.org/10.1016/j.rse.2015.06.004.

Dee, D.P., Uppala, S.M., Simmons, A.J., Berrisford, P., Poli, P., Kobayashi, S., Andrae, U., Balmaseda, M.A., Balsamo, G., Bauer, P., Bechtold, P., Beljaars, A.C.M., van de Berg, L., Bidlot, J., Bormann, N., Delsol, C., Dragani, R., Fuentes, M., Geer, A.J., Haimberger, L., Healy, S.B., Hersbach, H., Hólm, E.V., Isaksen, L., Kållberg, P., Köhler, M., Matricardi, M., Mcnally, A.P., Monge-Sanz, B.M., Morcrette, J.J., Park,

B.K., Peubey, C., de Rosnay, P., Tavolato, C., Thépaut, J.N., Vitart, F., 2011. The ERA-interim reanalysis: configuration and performance of the data assimilation system. Q. J. R. Meteorol. Soc. 137, 553–597. https://doi.org/10.1002/qj.828.

Farquhar, G.D., Wong, S.C., 1984. An empirical model of stomatal conductance. Funct. Plant Biol. 11, 191–210.

Farquhar, G.D., von Caemmerer, S., Berry, J.A., 1980. A biochemical model of photosynthetic CO2 assimilation in leaves of C3 species. Planta 149, 78–90. https://doi.org/10.1007/BF00386231.

Farruggia, A., Gastal, F., Scholefield, D., 2004. Assessment of the nitrogen status of grassland. Grass Forage Sci. 59, 113–120. https://doi.org/10.1111/j.1365-2494.2004.00411.x.

Feret, J.B., François, C., Asner, G.P., Gitelson, A.A., Martin, R.E., Bidel, L.P.R., Ustin, S.L., le Maire, G., Jacquemoud, S., 2008. PROSPECT-4 and 5: advances in the leaf optical properties model separating photosynthetic pigments. Remote Sens. Environ. 112, 3030–3043. https://doi.org/10.1016/j.rse.2008.02.012.

Flexas, J., Medrano, H., 2002. Drought-inhibition of photosynthesis in C3plants: stomatal and non-stomatal limitations revisited. Ann. Bot. 89, 183–189. https://doi.org/https://doi.org/10.1093/aob/mcf027.

Fourty, T., Baret, F., Jacquemoud, S., Schmuck, G., Verdebout, J., 1996. Leaf optical properties with explicit description of its biochemical composition: direct and inverse problems. Remote Sens. Environ. 56, 104–117. https://doi.org/10.1016/0034-4257(95)00234-0.

Frankenberg, C., Butz, A., Toon, G.C., 2011. Disentangling chlorophyll fluorescence from atmospheric scattering effects in O2 A-band spectra of reflected sun-light. Geophys. Res. Lett. 38, 1–5. https://doi.org/10.1029/2010GL045896.

Genty, B., Briantais, J.M., Baker, N.R., 1989. The relationship between the quantum yield of photosynthetic electron transport and quenching of chlorophyll fluorescence. Biochim. Biophys. Acta - Gen. Subj. 990, 87–92. https://doi.org/10.1016/S0304-4165(89)80016-9.

Gitelson, A.A., 2004. Wide dynamic range vegetation index for remote quantification of biophysical characteristics of vegetation. J. Plant Physiol. 161, 165–173. https://doi.org/10.1078/0176-1617-01176.

Gonzalez-Dugo, V., Durand, J.-L., Gastal, F., 2010. Water deficit and nitrogen nutrition of crops. A review. Agron. Sustain. Dev. 30, 529–544https://doi.org/10.1051/agro/2009059

Gonzalez-Dugo, V., Hernandez, P., Solis, I., Zarco-Tejada, P.J., 2015. Using high-resolution hyperspectral and thermal airborne imagery to assess physiological condition in the context of wheat phenotyping. Remote Sens. 7, 13586–13605. https://doi.org/10.3390/rs71013586.

Guan, K., Berry, J.A., Zhang, Y., Joiner, J., Guanter, L., Badgley, G., Lobell, D.B., 2016. Improving the monitoring of crop productivity using spaceborne solar-induced fluorescence. Glob. Chang. Biol. 22, 716–726. https://doi.org/10.1111/gcb.13136.

Guanter, L., Zhang, Y., Jung, M., Joiner, J., Voigt, M., Berry, J.A., Frankenberg, C., Huete, A.R., Zarco-Tejada, P., Lee, J.-E., Moran, M.S., Ponce-Campos, G., Beer, C., Camps-Valls, G., Buchmann, N., Gianelle, D., Klumpp, K., Cescatti, A., Baker, J.M., Griffis, T.J., 2014. Global and time-resolved monitoring of crop photosynthesis with chlorophyll fluorescence. Proc. Natl. Acad. Sci. 111, E1327–E1333. https://doi.org/10.1073/pnas.1320008111.

Gueymard, C., 1995. SMARTS2, A Simple Model of the Atmospheric Radiative Transfer of Sunshine: Algorithms and performance assessment. Publication Number: FSEC-PF-270-95. pp. 270–295.

Gueymard, C.A., Myers, D., Emery, K., 2002. Proposed reference irradiance spectra for solar energy systems testing. Sol. Energy 73, 443–467. https://doi.org/10.1016/S0038-092X(03)00005-7.

Harley, P.C., Loreto, F., Di Marco, G., Sharkey, T.D., 1992a. Theoretical considerations when estimating the mesophyll conductance to CO2 flux by analysis of the response of photosynthesis to CO2. Plant Physiol. 98, 1429–1436. https://doi.org/10.1104/pp.98.4.1429.

Harley, P.C., Thomas, R.B., Reynolds, J.F., Strain, B.R., 1992b. Modelling photosynthesis of cotton grown in elevated CO2. Plant Cell Environ. 15, 271–282. https://doi.org/10.1111/j.1365-3040.1992.tb00974.x.

He, L., Chen, J.M., Liu, J., Mo, G., Joiner, J., 2017. Angular normalization of GOME-2 Sun-induced chlorophyll fluorescence observation as a better proxy of vegetation productivity. Geophys. Res. Lett. 44, 5691–5699. https://doi.org/10.1002/2017GL073708.

Hernández-Clemente, R., North, P.R.J., Hornero, A., Zarco-Tejada, P.J., 2017. Assessing the effects of forest health on sun-induced chlorophyll fluorescence using the FluorFLIGHT 3-D radiative transfer model to account for forest structure. Remote Sens. Environ. 193, 165–179. https://doi.org/10.1016/j.rse.2017.02.012.

Houborg, R., Cescatti, A., Migliavacca, M., Kustas, W.P., Yang, X., Tang, J., Mustard, J.F., Lee, J., Rossini, M., Rascher, U., Alonso, L., Burkart, A., Cilia, C., Cogliati, S., Colombo, R., Damm, A., Drusch, M., Guanter, L., Hanus, J., Hyvärinen, T., Julitta, T., Jussila, J., Kataja, K., Kokkalis, P., Kraft, S., Kraska, T., Matveeva, M., Moreno, J., Muller, O., Panigada, C., Pikl, M., Pinto, F., Prey, L., Pude, R., Rossini, M., Schickling, A., Schurr, U., Schüttemeyer, D., Verrelst, J., Zemek, F., Houborg, R., Cescatti, A., Migliavacca, M., Kustas, W.P., Genty, B., Briantais, J.M., Baker, N.R., 2013. Satellite retrievals of leaf chlorophyll and photosynthetic capacity for improved modeling of GPP. Agric. For. Meteorol. 117, 10–23. https://doi.org/https://doi.org/10.1016/j.agrformet.2013.04.006.

Hu, J., Liu, L., Guo, J., Du, S., Liu, X., 2018. Upscaling solar-induced chlorophyll fluorescence from an instantaneous to daily scale gives an improved estimation of the gross primary productivity. Remote Sens. 10. https://doi.org/10.3390/rs10101663.

Huete, A.R., 1988. A soil-adjusted vegetation index (SAVI). Remote Sens. Environ. 25, 295–309. https://doi.org/10.1016/0034-4257(88)90106-X.

Huete, A., Didan, K., Miura, T., Rodriguez, E.P., Gao, X., Ferreira, L.G., 2002. MODIS_MOD13_NDVI_referenc. 83, 195–213. https://doi.org/10.1016/S0034-4257(02)00096-2.

Idso, S.B., 1982. Non-water-stressed baselines: a key to measuring and interpreting plant water stress. Agric. Meteorol. 27, 59–70. https://doi.org/10.1016/0002-1571(82)90020-6.

Idso, S.B., Jackson, R.D., Reginato, R.J., 1978. Extending the " degree day " concept of plant phenological development to include water stress effects author (s): Sherwood B . Idso , Ray D . Jackson , Robert J . Reginato published by : ecological Society of America Stable URL : http://www.jstor.org/s. Ecology 59, 431–433. https://doi.org/https://doi.org/10.2307/1936570.

Idso, S.B., Jackson, R.D., Pinter, P.J., Reginato, R.J., Hatfield, J.L., 1981. Normalizing the stress-degree-day parameter for environmental variability. Agric. Meteorol. 24, 45–55. https://doi.org/10.1016/0002-1571(81)90032-7.

Jackson, R.D., Idso, S.B., Reginato, R.J., Pinter, J.P.J., 1981. Canopy temperature as a crop water stress indicator. Water Resour. Res. 17, 1133–1138. https://doi.org/10.1029/WR017i004p01133.

Jacquemoud, S., Ustin, S.L., Verdebout, J., Schmuck, G., Andreoli, G., Hosgood, B., 1996. Estimating leaf biochemistry using the PROSPECT leaf optical properties model. Remote Sens. Environ. 56, 194–202. https://doi.org/10.1016/0034-4257(95)00238-3.

Jacquemoud, S., Verhoef, W., Baret, F., Bacour, C., Zarco-Tejada, P.J., Asner, G.P., François, C., Ustin, S.L., 2009. PROSPECT + SAIL models: a review of use for vegetation characterization. Remote Sens. Environ. 113, S56–S66. https://doi.org/10.1016/j.rse.2008.01.026.

Jones, H.G., Hall, D.O., Corlett, J.E., Massacci, A., 1995. Drought enhances stomatal closure in response to shading in sorghum (Sorghum bicolor) and in millet (Pennisetum americanum). Funct. Plant Biol. 22, 1–6.

Kipp, S., Mistele, B., Baresel, P., Schmidhalter, U., 2014. High-throughput phenotyping early plant vigour of winter wheat. Eur. J. Agron. 52, 271–278. https://doi.org/10.1016/j.eja.2013.08.009.

Kjeldahl, J., 1883. Neue Methode zur Bestimmung des Stickstoffs in organischen. J. Anal. Chem. 366–382. https://doi.org/https://doi.org/10.1007/BF01338151.

Koffi, E.N., Rayner, P.J., Norton, A.J., Frankenberg, C., Scholze, M., 2015. Investigating the usefulness of satellite-derived fluorescence data in inferring gross primary productivity within the carbon cycle data assimilation system. Biogeosciences 12, 4067–4084. https://doi.org/10.5194/bg-12-4067-2015.

Levula, J., Sabater, N., Mammarella, I., Vesala, T., Atherton, J., Drolet, G., Wade, T., MacLellan, C., Nichol, C., Middleton, E., Porcar-Castell, A., 2019. Diurnal and seasonal solar induced chlorophyll fluorescence and photosynthesis in a boreal scots pine canopy. Remote Sens.. 11, 273. https://doi.org/https://doi.org/10.3390/rs11030273.

Li, P., Wang, Q., 2011. Retrieval of leaf biochemical parameters using PROSPECT inversion: a new approach for alleviating ill-posed problems. IEEE Trans. Geosci. Remote Sens. 49, 2499–2506. https://doi.org/10.1109/TGRS.2011.2109390.

Meroni, M., Rossini, M., Guanter, L., Alonso, L., Rascher, U., Colombo, R., Moreno, J., 2009. Remote sensing of solar-induced chlorophyll fluorescence: review of methods and applications. Remote Sens. Environ. 113, 2037–2051. https://doi.org/10.1016/j.rse.2009.05.003.

Meroni, M., Busetto, L., Colombo, R., Guanter, L., Moreno, J., Verhoef, W., 2010. Performance of spectral fitting methods for vegetation fluorescence quantification. Remote Sens. Environ. 114, 363–374. https://doi.org/10.1016/j.rse.2009.09.010.

Moya, I., Camenen, L., Evain, S., Goulas, Y., Cerovic, Z.G., Latouche, G., Flexas, J., Ounis, A., 2004. A new instrument for passive remote sensing: 1. Measurements of sunlight-induced chlorophyll fluorescence. Remote Sens. Environ. 91, 186–197. https://doi.org/https://doi.org/10.1016/j.rse.2004.02.012.

Norton, A.J., Rayner, P.J., Koffi, E.N., Scholze, M., 2017. Assimilating solar-induced chlorophyll fluorescence into the terrestrial biosphere model BETHY-SCOPE: model description and information content. Geosci. Model Dev. Discuss. 1–26. https://doi.org/10.5194/gmd-2017-34.

Oleson, K.W., Dai, Y., et al., 2013. Technical Description of Version 4.5 of the Community Land Model (CLM). NCAR Technical Note NCAR/TN-503+STR 420. https://doi.org/https://doi.org/10.5065/D6RR1W7M.

Plascyk, J.A., Gabriel, F.C., 1975. The Fraunhofer line discriminator MKII an airborne instrument for precise and standardized ecological luminescence measurement. IEEE Trans. Instrum. Meas. 24, 306–313. https://doi.org/10.1109/TIM.1975.4314448.

Porcar-Castell, A., Tyystjärvi, E., Atherton, J., Van Der Tol, C., Flexas, J., Pfündel, E.E., Moreno, J., Frankenberg, C., Berry, J.A., 2014. Linking chlorophyll a fluorescence to photosynthesis for remote sensing applications: mechanisms and challenges. J. Exp. Bot. 65, 4065–4095. https://doi.org/10.1093/jxb/eru191.

Quebbeman, J.A., Ramirez, J.A., 2016. Optimal allocation of leaf-level nitrogen: implications for covariation of Vcmax and Jmax and photosynthetic downregulation. J. Geophys. Res. G Biogeosciences 121, 2464–2475. https://doi.org/https://doi.org/10.1002/2016JG003473.

Radin, J.W., Mauney, J.R., Guinn, G., 1985. Effects of N fertility on plant water relations and stomatal responses to water stress in irrigated cotton. Crop Sci. 25, 110–115. https://doi.org/10.2135/cropsci1985.0011183X002500010020x.

Rascher, U., Alonso, L., Burkart, A., Cilia, C., Cogliati, S., Colombo, R., Damm, A., Drusch, M., Guanter, L., Hanus, J., Hyvärinen, T., Julitta, T., Jussila, J., Kataja, K., Kokkalis, P., Kraft, S., Kraska, T., Matveeva, M., Moreno, J., Muller, O., Panigada, C., Pikl, M., Pinto, F., Prey, L., Pude, R., Rossini, M., Schickling, A., Schurr, U., Schüttemeyer, D., Verrelst, J., Zemek, F., 2015. Sun-induced fluorescence - a new probe of photosynthesis: first maps from the imaging spectrometer HyPlant. Glob. Chang. Biol. 21, 4673–4684. https://doi.org/10.1111/gcb.13017.

Rodriguez, D., Fitzgerald, G.J., Belford, R., Christensen, L.K., 2006. Detection of nitrogen deficiency in wheat from spectral reflectance indices and basic crop eco-physiological concepts. Aust. J. Agric. Res. 57, 781–789. https://doi.org/10.1071/AR05361.

Rouse, J.W., Hass, R.H., Schell, J.A., Deering, D.W., 1973. Monitoring vegetation systems

in the great plains with ERTS. In: Third Earth Resour. Technol. Satell. Symp. vol. 1. pp. 309–317. https://doi.org/citeulike-article-id:12009708.

Sellers, P.J., 1987. Canopy reflectance, photosynthesis, and transpiration. II. The role of biophysics in the linearity of their interdependence. Remote Sens. Environ. 21, 143–183.

Sharkey, T.D., Bernacchi, C.J., Farquhar, G.D., Singsaas, E.L., 2007. Fitting photosynthetic carbon dioxide response curves for C3 leaves. Plant Cell Environ. 30, 1035–1040. https://doi.org/10.1111/j.1365-3040.2007.01710.x.

Silva-Pérez, V., Furbank, R.T., Condon, A.G., Evans, J.R., 2017. Biochemical model of C3 photosynthesis applied to wheat at different temperatures. Plant Cell Environ. 40, 1552–1564. https://doi.org/10.1111/pce.12953.

Silva-Perez, V., Molero, G., Serbin, S.P., Condon, A.G., Reynolds, M.P., Furbank, R.T., Evans, J.R., 2018. Hyperspectral reflectance as a tool to measure biochemical and physiological traits in wheat. J. Exp. Bot. 69, 483–496. https://doi.org/10.1093/jxb/erx421.

Sitch, S., Smith, B., Prentice, I.C., Arneth, a., Bondeau, a., Cramer, W., Kaplan, J.O., Levis, S., Lucht, W., Sykes, M.T., Thonicke, K., Venevsky, S., 2003. Evaluation of ecosystem dynamics, plant geography and terrestrial carbon cycling in the LPJ dynamic global vegetation model. Glob. Chang. Biol. 9, 161–185. https://doi.org/https://doi.org/10.1046/j.1365-2486.2003.00569.x.

Smith, W.K., Biederman, J.A., Scott, R.L., Moore, D.J.P., He, M., Kimball, J.S., Yan, D., Hudson, A., Barnes, M.L., Macbean, N., Fox, A.M., Litvak, M.E., 2018. Chlorophyll fluorescence better captures seasonal and interannual gross primary productivity dynamics across dryland ecosystems of southwestern North America. Geophys. Res. Lett. 748–757. https://doi.org/10.1002/2017GL075922.

Thenkabail, P.S., Smith, R.B., De Pauw, E., 2000. Hyperspectral vegetation indices and their relationships with agricultural crop characteristics. Remote Sens. Environ. 71, 158–182. https://doi.org/10.1016/S0034-4257(99)00067-X.

van der Tol, C., Verhoef, W., Rosema, A., 2009a. A model for chlorophyll fluorescence and photosynthesis at leaf scale. Agric. For. Meteorol. 149, 96–105. https://doi.org/10.1016/j.agrformet.2008.07.007.

van der Tol, C., Verhoef, W., Timmermans, J., Verhoef, A., Su, Z., 2009b. An integrated model of soil-canopy spectral radiances, photosynthesis, fluorescence, temperature and energy balance. Biogeosciences 6, 3109–3129. https://doi.org/10.5194/bg-6-3109-2009.

van der Tol, C., Berry, J.A., Campbell, P.K.E., Rascher, U., 2014. Models of fluorescence and photosynthesis for interpretingmeasurements of solar-induced chlorophyll fluorescence. J. Geophys. Res. Biogeosci. 119, 2312–2327. https://doi.org/https://doi.org/10.1002/2014JG002713.

Uddling, J., Gelang-Alfredsson, J., Piikki, K., Pleijel, H., 2007. Evaluating the relationship between leaf chlorophyll concentration and SPAD-502 chlorophyll meter readings. Photosynth. Res. 91, 37–46. https://doi.org/10.1007/s11120-006-9077-5.

Verma, M., Schimel, D., Evans, B., Frankenberg, C., Beringer, J., Drewry, D.T., Magney, T., Marang, I., Hutley, L., Moore, C., Eldering, A., 2017. Effect of environmental conditions on the relationship between solar-induced fluorescence and gross primary productivity at an OzFlux grassland site. J. Geophys. Res. Biogeosci. 122, 716–733. https://doi.org/10.1002/2016JG003580.

Verrelst, J., Rivera, J.P., van der Tol, C., Magnani, F., Mohammed, G., Moreno, J., 2015. Global sensitivity analysis of the SCOPE model: what drives simulated canopy-leaving sun-induced fluorescence? Remote Sens. Environ. 166, 8–21. https://doi.org/10.1016/j.rse.2015.06.002.

Verrelst, J., van der Tol, C., Magnani, F., Sabater, N., Rivera, J.P., Mohammed, G., Moreno, J., 2016. Evaluating the predictive power of sun-induced chlorophyll fluorescence to estimate net photosynthesis of vegetation canopies: a SCOPE modeling study. Remote Sens. Environ. 176, 139–151. https://doi.org/10.1016/j.rse.2016.01.018.

Walker, A.P., Beckerman, A.P., Gu, L., Kattge, J., Cernusak, L.A., Domingues, T.F., Scales, J.C., Wohlfahrt, G., Wullschleger, S.D., Woodward, F.I., 2014. The relationship of leaf photosynthetic traits - Vcmax and Jmax - to leaf nitrogen, leaf phosphorus, and specific leaf area: a meta-analysis and modeling study. Ecol. Evol. 4, 3218–3235. https://doi.org/10.1002/ece3.1173.

Weis, E., Berry, J.A., 1987. Quantum efficiency of photosystem II in relation to 'energy'-dependent quenching of chlorophyll fluorescence. BBA - Bioenerg. 894, 198–208. https://doi.org/https://doi.org/10.1016/0005-2728(87)90190-3.

Wullschleger, S.D., 1993. Biochemical limitations to carbon assimilation in C3 plants—a retrospective analysis of the A/Ci curves from 109 species. J. Exp. Bot. 44, 907–920. https://doi.org/10.1093/jxb/44.5.907.

Yang, X., Tang, J., Mustard, J.F., Lee, J., Rossini, M., 2015. Geophysical Research Letter Supplementary Information for "Solar-Induced Chlorophyll Fluorescence Correlates with Canopy Photosynthesis on Diurnal and Seasonal Scales in a Temperate Deciduous Forest". pp. 2977–2987. https://doi.org/10.1002/2015GL063201. Received.

Yebra, M., Chuvieco, E., 2009. Linking ecological information and radiative transfer models to estimate fuel moisture content in the Mediterranean region of Spain: solving the ill-posed inverse problem. Remote Sens. Environ. 113, 2403–2411. https://doi.org/10.1016/j.rse.2009.07.001.

Zarco-Tejada, P.J., González-Dugo, V., Berni, J.A.J., 2012. Fluorescence, temperature and narrow-band indices acquired from a UAV platform for water stress detection using a micro-hyperspectral imager and a thermal camera. Remote Sens. Environ. 117, 322–337. https://doi.org/10.1016/j.rse.2011.10.007.

Zarco-Tejada, P.J., González-Dugo, M.V., Fereres, E., 2016. Seasonal stability of chlorophyll fluorescence quantified from airborne hyperspectral imagery as an indicator of net photosynthesis in the context of precision agriculture. Remote Sens. Environ. 179, 89–103. https://doi.org/10.1016/j.rse.2016.03.024.

Zhang, Y., Guanter, L., Berry, J.A., Joiner, J., van der Tol, C., Huete, A., Gitelson, A., Voigt, M., Köhler, P., 2014. Estimation of vegetation photosynthetic capacity from space-based measurements of chlorophyll fluorescence for terrestrial biosphere models. Glob. Chang. Biol. 20, 3727–3742. https://doi.org/10.1111/gcb.12664.

Zhang, Y., Guanter, L., Joiner, J., Song, L., Guan, K., 2018. Spatially-explicit monitoring of crop photosynthetic capacity through the use of space-based chlorophyll fluorescence data. Remote Sens. Environ. 210, 362–374. https://doi.org/10.1016/j.rse.2018.03.031.

Zheng, T., Chen, J., He, L., Arain, M.A., Thomas, S.C., Murphy, J.G., Geddes, J.A., Black, T.A., 2017. Inverting the maximum carboxylation rate (Vcmax) from the sunlit leaf photosynthesis rate derived from measured light response curves at tower flux sites. Agric. For. Meteorol. 236, 48–66. https://doi.org/10.1016/j.agrformet.2017.01.008.

Zweifel, R., Bohm, J.P., Hasler, R., 2002. Midday stomatal closure in Norway spruce–reactions in the upper and lower crown. Tree Physiol. 22, 1125–1136. https://doi.org/10.1093/treephys/22.15-16.1125.